DTU Health Tech
Department of Health Technology

Development of a Wearable EEG Device for Continuous Long-Term Monitoring Using Conductive Polymers as Electrodes

Master Thesis

Development of a Wearable EEG Device for Continuous Long-Term Monitoring Using Conductive Polymers as Electrodes

Master Thesis
April, 2025

By
Xuanqin Yu

Copyright: Reproduction of this publication in whole or in part must include the customary bibliographic citation, including author attribution, report title, etc.
Cover photo: Vibeke Hempler, 2012
Published by: DTU, Department of Health Technology, Brovej, Building 423, 2800 Kgs. Lyngby Denmark
https://www.healthtech.dtu.dk/
ISSN: [0000-0000] (electronic version)
ISBN: [000-00-0000-000-0] (electronic version)

ISSN: [0000-0000] (printed version)
ISBN: [000-00-0000-000-0] (printed version)

Approval

This thesis has been prepared over five months at the Department of Health Tech, Technical University of Denmark, (DTU) in partial fulfillment for the degree Master of Biomedical engineering, MSc Eng.

It is assumed that the reader has a basic knowledge in the areas of electronics, biomedical signal processing and computer science.

Xuanqin Yu - s222456

.....

Signature

.....

Date

Abstract

Electroencephalography (EEG) plays a crucial role in neurological diagnosis and brain science research with its affordability, easy-to-use property, and high temporal resolution. However, traditional EEG devices in hospital have limitations in wearability, making them unsuitable for various conditions such as exercise, driving, and home-based monitoring. While some wearable EEG devices which are available on the market, still face challenges related to limited battery life, making them unsuitable for long-term continuous monitoring such as sleeping study. This thesis presents the development of a wearable EEG device with long-term monitoring capability, focusing on circuit design, low-power optimization, and real-world EEG signal acquisition experiments. Additionally, the potential use of conductive polymer materials as biomedical signal electrodes is assessed alongside traditional EEG electrodes, aiming to improve signal quality and enhance the convenience of EEG monitoring.

To achieve flexibility and high signal quality, the hardware design carefully balances the size and function of components. The amplification circuit consists of two stages: an instrumentation amplifier providing a gain of approximately 40 dB, followed by the second amplifier offering a gain of 45 or 50 dB. The filtering circuit includes a 50 Hz notch filter, a 0.5 Hz high-pass filter, and a 70 Hz low-pass filter. The signal is then digitized using an 18-bit ADC and transmitted to a computer via Bluetooth. Additionally, a Driven Right Leg (DRL) circuit is implemented to increase the common-mode rejection ratio (CMRR) and improve signal quality. Firmware-level low-power optimization is applied to extend battery life up to 200 hours with a 3.7V Li-ion battery.

The software of the device focuses on the optimization of the power consumption. The main micro-computer unit (MCU) is programmed using industry-level developing tools, result tremendous improvement in battery life compared with other wearable EEG device. The data is transmitted through Bluetooth Low Energy (BLE), and available to wireless change the sample mode about channel numbers and sample rate from computer. The signal is stored and visualized using a python script, and further signal processing method like digital filtering and Fast Fourier Transformation are applied to assist analysis.

To evaluate the performance of the device and different electrode materials, including conductive polymer electrodes, gradual and effective experiments were conducted. The results show that the device successfully provides clear and readable EEG signals when using standard medical electrodes. However, the performance of the conductive polymer material was not satisfying. Potential issues are discussed, and further research is needed to improve this material for EEG applications.

Finally, this thesis demonstrates that careful design and optimization, integrating both hardware and software, can result in a practical and efficient wearable EEG device for long-term continuous monitoring. Future work will focus on further miniaturization of the device and the enhancement of conductive polymer electrodes for biomedical signal acquisition.

Acknowledgements

Xuanqin Yu, MSc Biomedical Engineering, DTU
Writer of the thesis.

Alireza Dolatshahi Pirouz, Associate Professor, Department of Health Technology
Group leader of the Biologically Inspired Material Engineering, special thanks for the lending of the innovative conductive polymer material and technical support.

Sadasivan Puthusserypady Kumaran, Associate Professor, Department of Health Technology
Group leader of the Biomedical Signal Processing, I'm gratitude for the advice and feedback in development.

Tiberiu Gabriel Zsurzsan, Associate Professor, Department of Electrical and Photonics Engineering
Thanks to the help for the advice in electronics part of the design.

Morteza Alehosseini , Postdoc, Department of Health Technology
Deepest appreciation for the regulation of the whole project, helpful advices and regular feedbacks.

Speicial thanks to the Cihan Uyanik who provided the regular electrodes and conductive gel for the signal acquisition and comparement.

Contents

Preface . . . ii
Abstract . . . iii
Acknowledgements . . . iv

1 Introduction **1**
1.1 Electroencephalography (EEG) and Its Applications . . . 1
1.2 Motivation and Objectives . . . 5
1.3 Content Structure . . . 6

2 Background **9**
2.1 EEG Signal Acquisition Principle . . . 9
2.2 EEG electrode . . . 12

3 System Overview **15**

4 Hardware Design **19**
4.1 Amplification Circuit . . . 19
4.2 Filtering . . . 28
4.3 ADC . . . 35
4.4 Power Management . . . 38

5 Software and MCU **41**
5.1 MCU . . . 41
5.2 Bluetooth . . . 43
5.3 Python-based Visualization and Processing . . . 45

6 Low Power Optimization **47**
6.1 ESP32 procedure . . . 47
6.2 I2C in Assembler . . . 48

7 Experiment and result **53**
7.1 Experiment 1: EEG Signal Acquisition . . . 53
7.2 Experiment 2: Electrodes comparison . . . 57
7.3 Experiment 3: Battery life . . . 59

8 Discussion **61**
8.1 Result analysis . . . 61
8.2 Future . . . 62

9 Conclusion **65**

Bibliography **67**

A Appendix **71**
A.1 ulp.S . . . 71

1 Introduction

1.1 Electroencephalography (EEG) and Its Applications

Electroencephalography (EEG) is a widely used non-invasive technique for monitoring brain activity by placing multiple electrodes on the scalp, whose locations are based on the functional brain area under the scalp[1]. These electrodes measure the small voltage differences—typically in the microvolt range—between a reference electrode and a signal electrode[2]. The traditional application of EEG is in hospital neurology departments, playing a crucial role in epilepsy diagnosis and other neurological studies. While recently, with the increasing popularity of brain science, brain-computer interfaces (BCI) and advanced algorithms in deep learning, EEG has obtained attention in academic domain with advantages in high temporal resolution, low cost, and simple setup procedure, compared to other neuralimaging techniques such as electrocorticography (ECoG), in vivo electrodes, or magnetic resonance imaging (MRI)[3]. Today, EEG has become one of the most common, easiest and cheapest technique to study the brain.

Traditional EEG Systems in Hospitals
A conventional hospital-level EEG system meeting the recording standards of International Federation of Clinical Neurophysiology [4] consists of several key components in fig. 1.1:

- **Electrode System** – This typically includes an electrode cap, Gold or Ag/AgCl cup electrodes applied with electrode paste or gel, and shielded electrode leads. The electrode cap is a lightweight fabric or gauze-based cap with precisely arranged openings to expose the electrode locations, following the International 10-20 system. This standardized system ensures that EEG recordings are consistent across different individuals and studies[5].

  During setup, a clinician applies conductive gel to the scalp through the cap openings before placing Ag/AgCl electrodes. This arrangement forms a layered structure consisting of metal, gel, and skin, ensuring optimal conductivity[6]. The electrodes are then connected to the signal acquisition unit via shielded leads. In standard clinical EEG examinations, 16 to 25 electrodes are used to capture entire brain activity in different regions.

- **Signal Acquisition and Processing Unit** – This is the core of an EEG device. It amplifies the weak microvolt-level EEG signals to the millivolt or even volt range before digitizing them using an analog-to-digital converter (ADC). Each EEG channel has its own amplification and filtering circuits, which contribute to the overall size, power consumption, and cost of the device. The digitized signals are then transmitted to a computer via USB cable for further processing.

- **User Interface (UI) and Analysis Software** – The processed EEG data is displayed on a computer screen, where specialized software tools perform various analyses, including spectrogram, artifact removal, and event recognition (e.g., epilepsy detection)[7][8][9]. Additional auxiliary devices may also be used, such as video recording equipment or stimulation tools that trigger brain responses using light or sound for research.

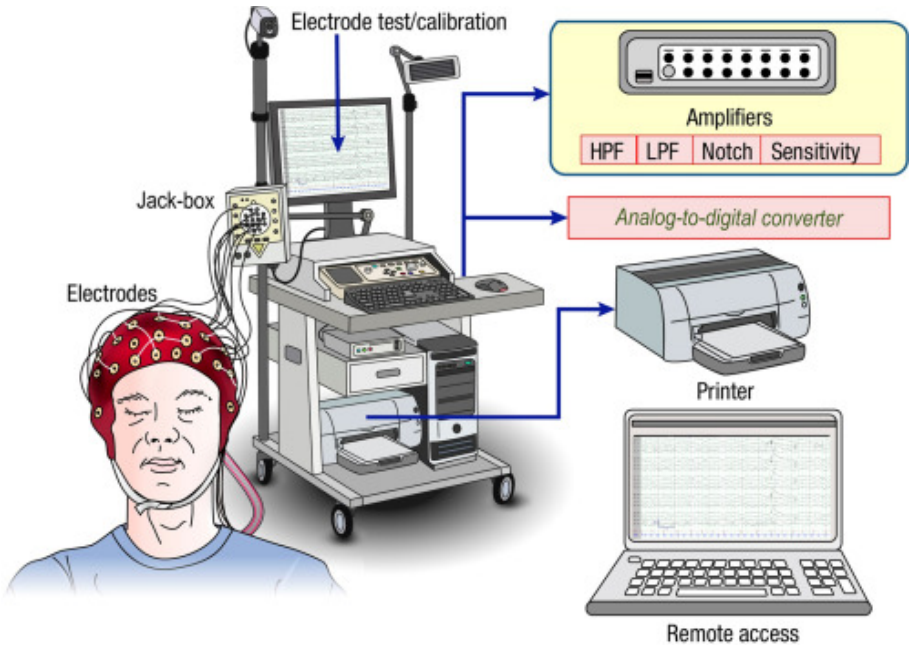

Figure 1.1: Traditional EEG equipment in hospital [10].

EEG in Brain Science and BCI

Although EEG is widely used in medical domain, its applications are expanding to non-medical fields, particularly in brain science and BCI. As shown in fig. 1.2, the number of publications using EEG on non-medical area has been steadily increasing since 2017, showing its growing popularity among researchers [3]. Additionally, EEG applications in non-medical areas—such as attention detection, motion imagery recognition, and cognitive state monitoring are becoming more popular[11][12][13], revealing the great prospect of EEG technique. Especially with the development of the deep learning, the analyzation of EEG signal, the complex time series data that are hard to understand by human becomes easier to learn. The common EEG-based research techniques can generally be classified into two categories[3]:

The active (positive) EEG techniques involve EEG responses triggered by specific actions or stimuli. Depending on different types of stimuli, example includes: Auditory evoked potentials, where the brain activity changes in response to sound stimuli at specific frequencies. Motor imagery, in which EEG detects activity in brain regions responsible for movement, even when no actual movement occurs. And for imaginary speech processing, EEG signals are analyzed to recognize imagined speech patterns[12].

Another category is the passive (negative) EEG techniques. These focus on spontaneous changes in EEG signals without direct external stimuli. For example, EEG can quantify cognitive states such as attention, drowsiness, and emotional responses[13], making it useful for applications like fatigue monitoring, adaptive learning, and building the feedback systems.

Both types of EEG applications hold significant potential for academia and industry.

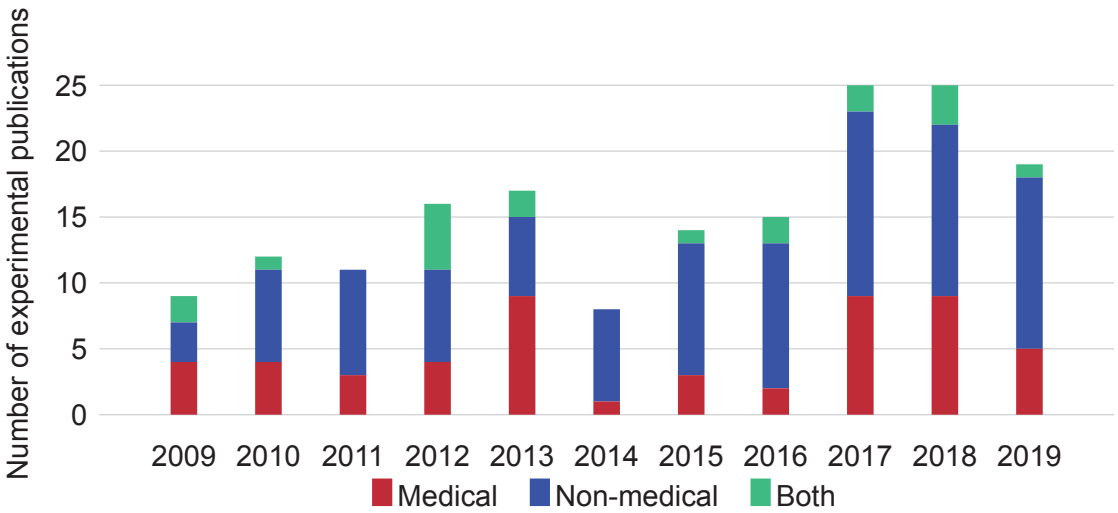

Figure 1.2: Experimental publications using EEG per year covering the period from January 2009 to October 2019, remade from [3].

1.1.1 Advantages of EEG

EEG is favored by researchers for several reasons[6]:

- **Cost-Effectiveness** – EEG systems are significantly more affordable than other neuroimaging techniques like MRI. Even when commercial medical-level EEG devices are too expensive for a lab, researchers can develop their own low-cost EEG systems and record the satisfying signals.

- **Non-Invasive Method** – Unlike invasive procedures, EEG does not require surgical implantation, reducing health risks and complications. And it is a passive method, so it is safe to use on human.

- **Compatibility with Other Methods** – EEG is a passive recording technique, meaning it does not interfere with other imaging methods. It is often used alongside functional magnetic resonance imaging (fMRI), magnetoencephalography (MEG), and near-infrared spectroscopy (NIRS) to provide complementary insights of brain activity.

- **High Temporal Resolution** – Since EEG measures voltage fluctuations on the scalp in real-time, it offers very high time resolution compared to many other imaging techniques (fig. 1.3). However, its spatial resolution is lower due to the interference caused by the skull, scalp tissues and even signal origination[14].

Despite its limitations, EEG remains a powerful and versatile tool for neuroscience research, clinical diagnostics, and it is still an emerging applications in BCI.

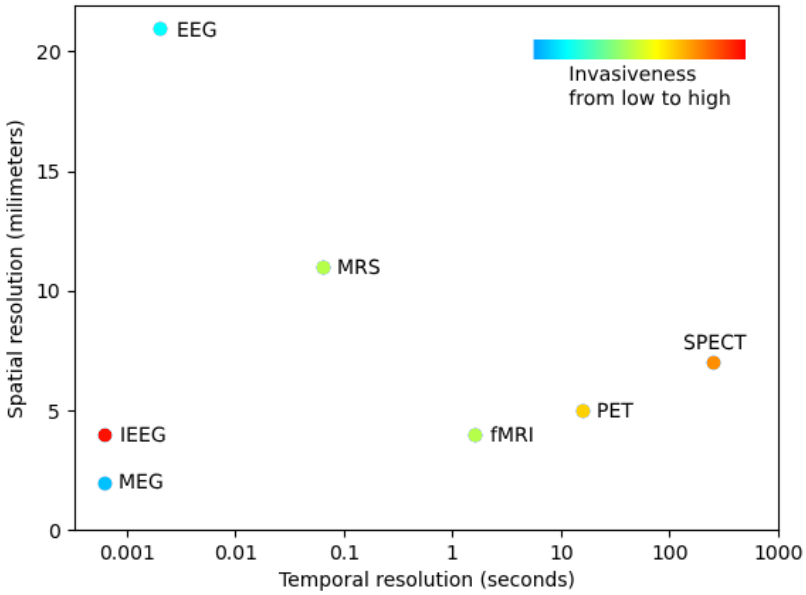

Figure 1.3: The temporal and spacial resolution of the common invasive and non-invasive techniques in BCI, remade from [14].

1.1.2 Limitation of Current EEG Device

table 1.1 presents several medical-level EEG devices available on the market. Advanced device typically support 24 to 32, and up to 256 channels, with sampling frequencies ranging from 2 to 16 KHz. These devices are usually priced at 30,000 Krone or higher. And most of them rely on wired connections, making the system bulky and often fixed in place, primarily for routine examinations and research. This setup restricts their use in specialized conditions such as exercise, driving, or sleep, areas with significant potential for both applications and research. Thus, the **first major limitation of current medical EEG devices is their lack of flexibility for complex research environments**.

Table 1.1: Example of hospital-used EEG device. The latest price is referred from price history in Bimedis.

	Nihon Kohden Neurofax EEG1200	Natus Medical Natus Quantum	Micromed BRAIN QUICK	Compumedics Grael 4K-EEG
Channels	256	256	32	32
Fs/Hz	2000	16 000	4400	16 384
Resolution/bits	24	24	24	24
Price/$	4150	4600	5250	1212

As a result, there is a growing demand for wearable EEG devices, which have become a popular research focus[15]. table 1.2 summarizes the state-of-the-art commercial wearable EEG devices available in 2018. Wearable EEG devices often support up to 24 or 32 channels, similar to medical-level devices, but their sampling frequencies are typically lower, ranging from 500 to 1000 Hz. These devices are compact, often designed as an 80 × 52 × 12 mm³ rectangular box secured to the scalp with a headband. However, their

battery life is generally limited to 5–8 hours, preventing continuous monitoring for a full 24-hour period. **Therefore, the second limitation of current EEG devices is their inability to support long-term continuous recording over multiple days**.

Table 1.2: Example of state-of-art commercially available EEG units which are wearable and present only on the head, remade from [16].

	mBrainTrain Smarting	Brian Products LiveAmp	g.tec g.Nautilus	Cognionics Mobile-128	Emotic Epoc Flex
Channels	24	32	32	128	32
Fs/Hz	500	1000	500	1000	128
Resolution/bits	24	24	24	24	14
Size/mm	81x52x12	83x51x14	-	-	-
Weight/g	60	60	-	460	-
Battery life/h	5	3	8	6	9

For long-term monitoring, another critical issue is the electrodes. Traditional wet/gel electrodes require the application of conductive gel to the scalp, which can cause discomfort, allergic reactions, and requires complicated preparation and cleanup time. Furthermore, over extended use, the gel gradually dries out, the increased impedance reduces the signal quality, demanding a frequent reapplication[15]. To address this, some researchers have explored the use of dry electrodes in wearable EEG devices. However, dry electrodes also present challenges, such as discomfort from mechanical pressure, particularly during sleep, as well as increased susceptibility to movement artifacts and powerline interference[4]. As a result, **inconvenient electrode-related challenges represent the third major limitation of current EEG device**.

1.2 Motivation and Objectives

To address the three main limitations of current commercial EEG devices before: lack of flexibility, limited battery life, and complex electrode setup, this study aims to develop a wearable EEG device capable of long-term continuous monitoring using easy-to-use conductive polymer electrode. The device will be designed, fabricated, and tested from scratch, covering all aspects including circuit design, component selection and comparison, programming, and power system optimization. Additionally, the study will include experimental design, technical verification, and performance evaluation of different electrode materials.

To address the first limitation, flexibility, the device design focuses on three key aspects:

- Size and Weight – In hospital devices, EEG signal processing units are typically powered through cables connected to computers or large battery packs, making them impractical for wearable applications. Commercial wearable EEG devices, such as those from NeuroSky and Zeo[17], are often compact, attached to headbands, and comparable in size to a matchbox. Inspired by these designs, our device will minimize PCB component size while remaining essential EEG signal processing elements.
- Battery System – Traditional biomedical signal processing circuits, including EEG systems, often require dual power supplies, that are powered by two batteries. However, recent advancements in 3.7V rechargeable Li-Po batteries offer higher capacity in a compact form, making them ideal for flexible applications. Our device will

integrate a Li-Po battery with a power management circuit, providing the necessary dual power supply for op amps while ensuring stable voltage for the MCU.

- Wireless Communication – Reducing the number of cables is helpful to the usability and comfort of wearable EEG devices. Therefore, our design will incorporate wireless data transmission, minimizing the need for physical connections.

The second limitation, battery life as outlined in table 1.2, is addressed by optimizing power consumption. The objective is to increase the battery life to over at least 24 hours. Our design reduces the number of EEG channels to four, which is sufficient for many research applications while significantly saving space in PCB board[18]. Sampling frequency and ADC resolution will be carefully selected for efficiency. Additionally, specific power optimization techniques will be applied to the MCU, which is the main power consumption source, prolonged the battery life tremendously.

Finally, the third limitation, related to electrodes, involves the test of a new conductive polymer material for EEG electrode, which presents great attachment to the skin and soft physical properties. Traditional wet/gel electrodes, dry electrodes, and conductive polymer electrodes will be compared in terms of impedance and overall signal quality. The advantages and disadvantages of the new conductive polymer electrodes will be discussed based on experimental results.

1.3 Content Structure

This thesis is structured into nine chapters, each addressing different aspects of the development of the wearable, low-power EEG device utilizing conductive polymer electrodes. The structure is designed to systematically introduce the background, design methodology, experimental evaluation, and findings. The organization is as follows:

- **Chapter 1**: Introduction outlines the motivation behind the research, the research objectives, and the contributions of this study. It also provides a brief overview of the thesis structure.
- **Chapter 2**: Background of the EEG signal presents a review of the fundamental concepts of EEG signal acquisition and electrode materials. It also discusses the potential of conductive polymers in EEG applications.
- **Chapter 3**: System Design Overview provides a high-level overview of the proposed EEG system, including the key design requirements and system architecture. It introduces the major hardware and software components used in the device.
- **Chapter 4**: Hardware Design details the design and implementation of the analog front-end, including the building of instrumental amplifier, filter circuits, and the ADC. Additionally, power management strategies to ensure long-term operation are discussed.
- **Chapter 5**: Software & Embedded System describes the firmware development for the microcontroller unit (MCU), including communication with the ADC and wireless data transmission using Bluetooth. It also outlines the strategies employed to minimize power consumption through optimized sleep modes and communication protocols.
- **Chapter 6**: Low-Power Optimization focuses on power efficiency improvements, particularly in optimizing the MCU strategy and procedure design. This includes the implementation of an I2C communication protocol in assembly language to mini-

mize energy consumption. Experimental measurement of power consumption after optimization is presented.

- **Chapter 7**: Experimental Setup & Results describes the experimental methodology used to evaluate both EEG signal quality and power efficiency. A gradient experiment confirms the efficiency of the device and it provides results comparing conductive polymer electrodes with conventional electrodes.
- **Chapter 8**: Discussion & Future Work interprets the experimental results and discusses their implications. It also outlines potential future improvements, such as further miniaturization of the system and evaluation on the conductive polymer material.
- **Chapter 9**: Conclusion summarizes the key findings and contributions of this research and highlights directions for future developments in wearable EEG technology.

Finally, References & Appendices include citations for all referenced literature and supplementary materials such as circuit schematics and relevant code in Github Repository [19]. This structured approach ensures that the thesis provides a comprehensive and logical flow, enabling readers to understand the research process, methodology, and key contributions effectively.

2 Background

2.1 EEG Signal Acquisition Principle

2.1.1 EEG generation

Electroencephalography (EEG) is a non-invasive technique for recording the brain electrical activity by measuring potential differences between two points on the scalp. EEG signals primarily reflect the synaptic potentials of pyramidal neurons in the neocortex and allocortex. In fig. 2.1, the electrical activity generated in the cortex propagates through various biological tissues, including muscle and bone before reaching the scalp, where it is captured by electrodes. Conventional scalp or cortical surface–recorded EEG is unable to record the single neuronal action potentials. Actually, the neural activity detectable by the EEG is the summation of the excitatory and inhibitory postsynaptic potentials of relatively large groups of neurons firing synchronously[6], thus the spatial resolution of the EEG device is not so high. Before the signal reaches to the electrode, there are also many noise from surround such as powerline interference or accompanied EMG signals.

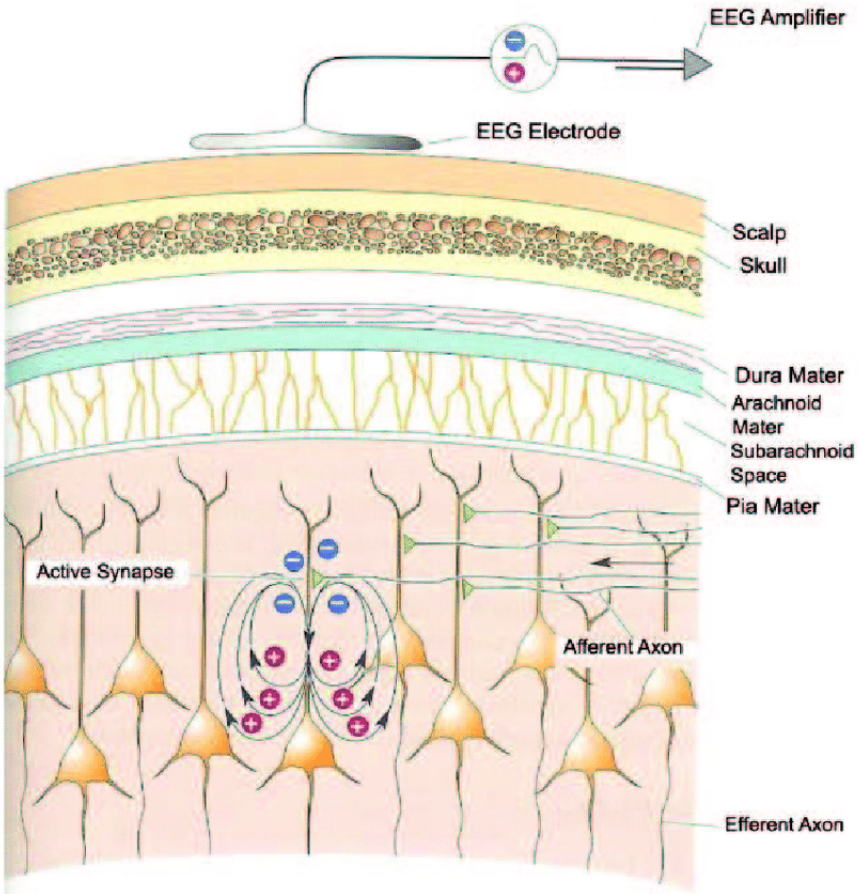

Figure 2.1: The transmission of the EEG signal from the a group of neurons firing synchronously to the electrode on skin.

2.1.2 International 10-20 system

The placement of electrodes significantly influences EEG recordings, as different brain regions exhibit distinct electrical activity patterns. The most widely adopted system for electrode placement is the International 10-20 System (fig. 2.2) commonly used in clinical, research, and laboratory settings[5]. The ”10” and ”20” in its name refer to the relative distances between adjacent electrodes, which are either 10% or 20% of the total head circumference from front to back or left to right. This standardized placement ensures consistency, reproducibility, and comparability across EEG studies.

Electrode positions are named based on the underlying brain region, using prefixes such as: Fp (prefrontal lobe), F (frontal lobe), T (temporal lobe), P (parietal lobe), O (occipital lobe). Additionally, C denotes the center of the scalp, A represents the auricular (ear) electrodes, and M sometimes refers to the mastoid bone. Electrode positions are further specified using numbers: even numbers (2, 4, 6, 8) indicate the right side of the head (from a top-down view), while odd numbers indicate the left side. Electrodes placed closer to the midline are assigned smaller numbers, and the midline itself is labeled as Z (e.g., Fz, Cz, Pz).

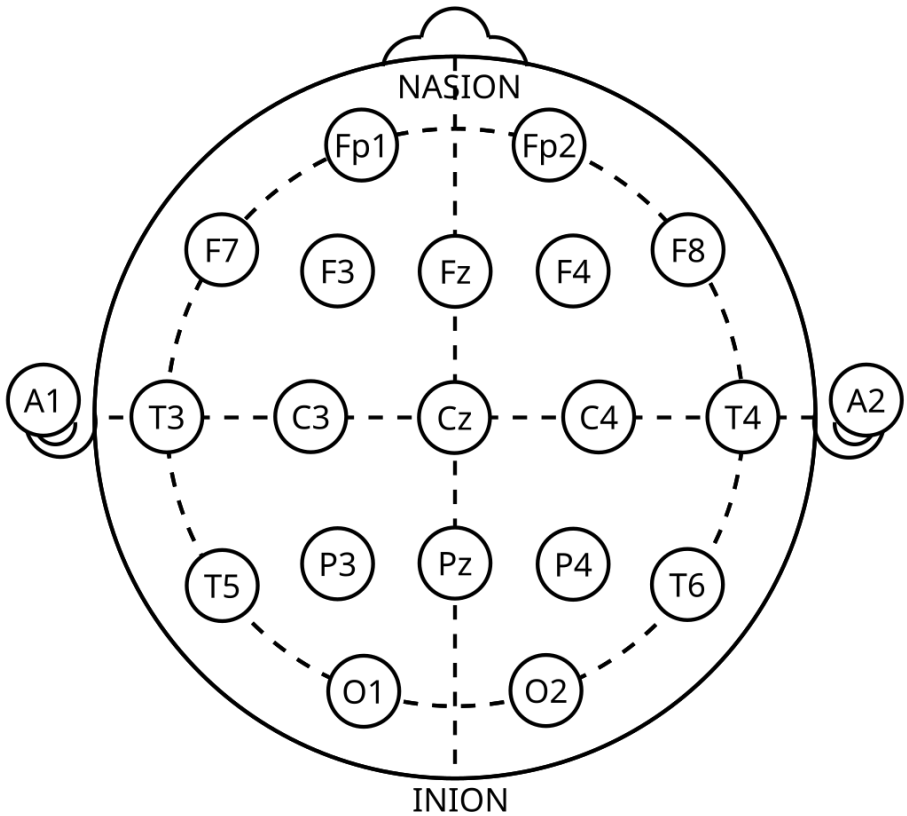

Figure 2.2: The top view of set up followed by international 10-20 system.

In basic polysomnography, common electrodes include F3, F4, Fz, Cz, C3, C4, O1, O2, A1, and A2 (M1, M2). The Fz and Cz electrodes often serve as common references, while A1 and A2 are frequently used as ground electrodes. Unlike electrocardiography (ECG) or electromyography (EMG), which use distant reference electrodes (e.g., placed on the legs), EEG reference electrodes are often positioned on the scalp and can changed depend on the study. Signals can be measured in various configurations, such as Fp2-O2, where the potential difference is recorded between Fp2 and O2: $V(Fp_2) - V(O_2)$. Some

studies further refine EEG signals by computing an average reference from all electrodes to represent the brain's overall potential, aiding in computational analyses for applications like sleep studies and epilepsy detection[6].

To ensure precise electrode placement, anatomical landmarks such as the nasion (the depression between the eyes, above the nose bridge) and the inion (a prominent point at the back of the skull) are used. A line connecting these points is divided into segments (10%-20%-20%-20%-10%) to determine locations for Fpz, Fz, Cz, Pz, and Oz electrodes. Similarly, electrodes along the transverse axis are positioned at proportional intervals between the preauricular points (ear level), ensuring uniform coverage of the scalp.

2.1.3 Electrical characteristics of EEG

EEG signals represent one-dimensional electrical potential differences measured between electrode pairs. In healthy individuals, EEG amplitude typically ranges from 20 to 100 μV, with frequencies spanning 0.5 to 70 Hz[2]. Compared to ECG (0–1 mV) and EMG (up to hundreds of millivolts), EEG signals are extremely weak. In additional, since EEG does not have obvious characteristic like the QRS wave and RT segment in ECG, it is hard to discriminate the EEG signal with noise in temporal domain, but in frequency domain it is different.

In fig. 2.3, the EEG frequency spectrum can be divided into distinct wave types, each associated with specific brain states[7][6][20]:

- **Alpha waves (8–12 Hz):** Predominantly recorded at the parietal and occipital lobes in a relaxed, wakeful state. Their amplitude decreases when the eyes are opened.
- **Beta waves (12–30 Hz):** Typically associated with active thinking, problem-solving, and alertness.
- **Delta waves (0.5–4 Hz):** Common during deep sleep (stages N3), especially in the frontal and central regions. Presence during wakefulness may indicate pathology.
- **Theta waves (4–8 Hz):** Observed during light sleep (stages N1 and N2) and emotional states. They are most prominent in the frontal and central regions and gradually shift toward the occipital lobe as sleep progresses.

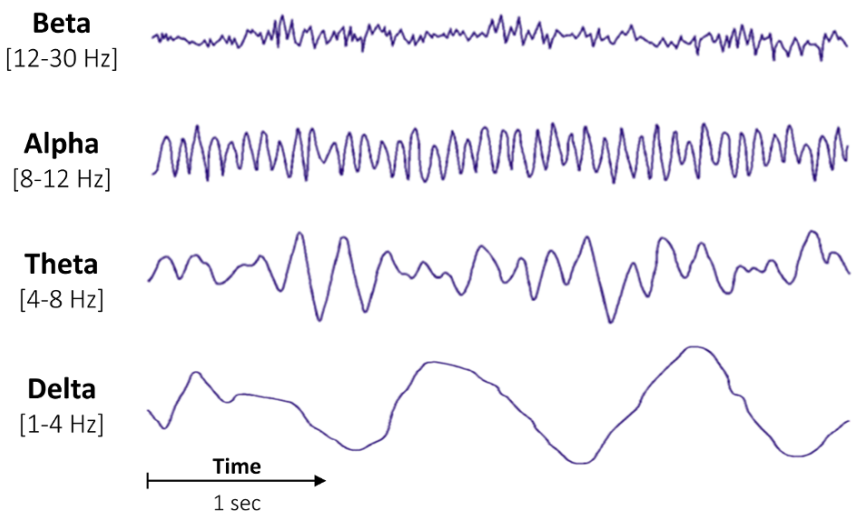

Figure 2.3: Common waveforms of EEG in health people.

In some state-of-art research, a specialized EEG rhythm, the Mu wave, shares a frequency range with alpha waves but exhibits a distinct arch-like morphology, is studied[20]. It typically appears when an individual contemplates a movement of a contralateral limb, making it useful for brain-computer interface (BCI) applications.

In pathological conditions, EEG signal characteristics may change significantly. High-Frequency Oscillations (HFOs) are components above 30 Hz, categorized into[20]:

- **Gamma waves (30–80 Hz):** Associated with sensory perception and cognitive processing.
- **Ripples (80–200 Hz):** Implicated in memory consolidation and neuronal communication.
- **Fast ripples (200–500 Hz):** Often linked to epileptic activity and neural hyperexcitability.

Recent studies suggest that gamma oscillations play a crucial role in integrating sensory information across brain regions. In contrast, fast ripples have been investigated as potential biomarkers for epilepsy, motor activity interference, and drug-induced neural alterations[20].

2.2 EEG electrode

The most commonly used electrodes for EEG signal acquisition are wet (gel-based) electrodes, which are also widely applied in ECG and EMG recordings. A typical wet electrode consists of a foam gasket to paste the electrode to the skin, an Ag/AgCl metal electrode to detect voltage changes, and a conductive gel to reduce skin-electrode impedance and improve signal quality. The hydrogel facilitates the conversion between ionic and electronic currents, ensuring low electrode-skin impedance, typically around 1 kΩ[21]. In fig. 2.4, the electrode and skin can be modeled as an electronic circuit. In research and clinical EEG devices, cup electrodes are more commonly used. These dish-shaped electrodes, usually made of gold or Ag/AgCl, are filled with conductive gel and attached to the scalp for stable recordings. The International Federation of Clinical Neurophysiology recommends that the impedance of electrode should be less than 5 kΩ to ensure the high quality EEG signal, but with exquisite modern amplification circuit design, higher impedance electrode over 10 kΩ can also reserve high quality signal[4].

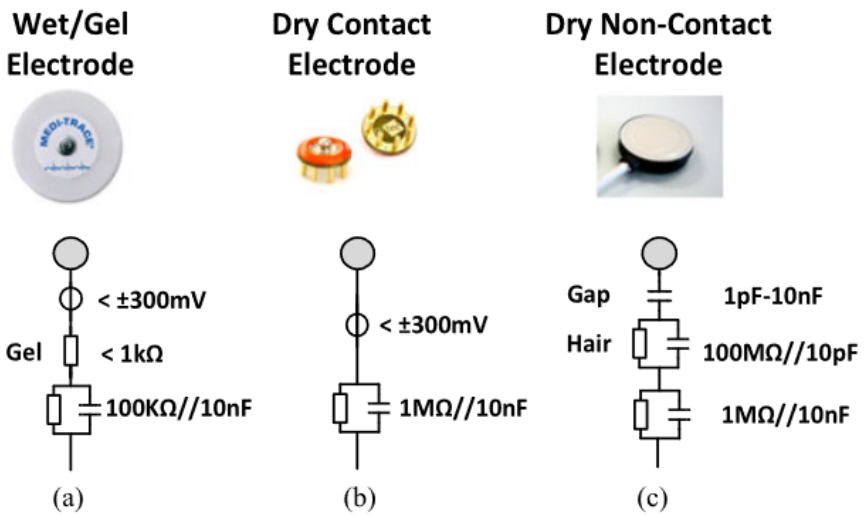

Figure 2.4: Common EEG electrode and their electronics circuit model, the Wet/Gel Electrode presents the least impedance.

Despite their effectiveness, wet electrodes are not ideal for long-term, continuous EEG monitoring since the gel dries out over time, leading to signal degradation[15]. Dry electrodes solve this issue but come with trade-offs: They exhibit high electrode-skin impedance, often in the range of hundreds of kiloohms to tens of megaohms, resulting in increased noise and interference[21]. However, they offer faster setup, improved comfort, and reduced hair interference compared to wet electrodes.To mitigate noise in dry electrodes, researchers have explored minimizing the distance between the electrode and amplifier, increase gain and denoising method.

With the development of the material science, especially the application of the graphene, metal are not the only conductive material used in electrode. Recently a new conductive polymer material called CareGum caught our attention, it is a hydrogel made mainly of fibroin protein (derived from natural silk) and graphene oxide, which are conductive, self-healing, stretchable, and biocompatible [22][23]. These fantastic properties make it possible to be extensively used in biomedical sensors. In fig. 2.5, the conductive polymer is available for the simple direct current example using LED, and the resistor of the material is around 100 kΩ in stable condition. In out device, the conductive polymer electrode will be tested to verify its potential as the EEG electrode.

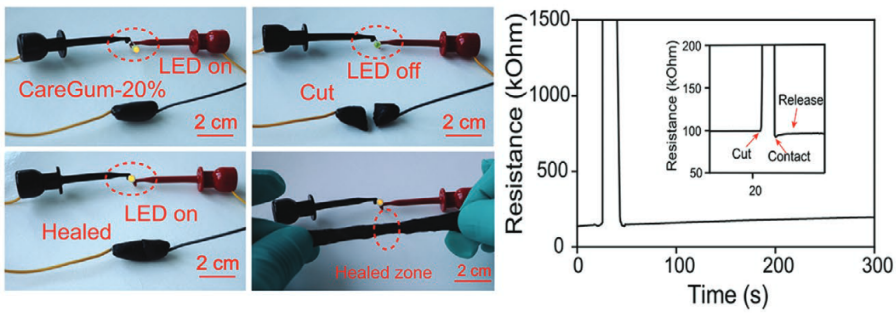

Figure 2.5: The conductivity of the conductive polymer in a LED circuit, the right figure shows the resistor of material is around 100 kΩ[23].

3 System Overview

fig. 3.1 illustrates the complete design of the device, which consists of four channels. Each channel features an identical amplification circuit, except for the first channel which includes an additional Driven Right Leg (DRL) circuit to suppress common-mode noise through feedback. The amplification circuit comprises an instrumentation amplifier (INA333, Texas Instruments), a 50 Hz notch filter, a high-pass filter (HPF) with a 0.5 Hz cutoff frequency, a low-pass filter (LPF) with a 70 Hz cutoff frequency, a second active amplifier, and a DC offset circuit. All operational amplifiers (op-amps) used in this stage are of the same type (OPA2333, TI). Then analog signal is sampled at 250 Hz or 100 Hz and converted into 16-bit digital signal. The choose of filtering frequency range and sample frequency follows the International Federation of Clinical Neurophysiology's recommendation for routine and sleep EEG[4].

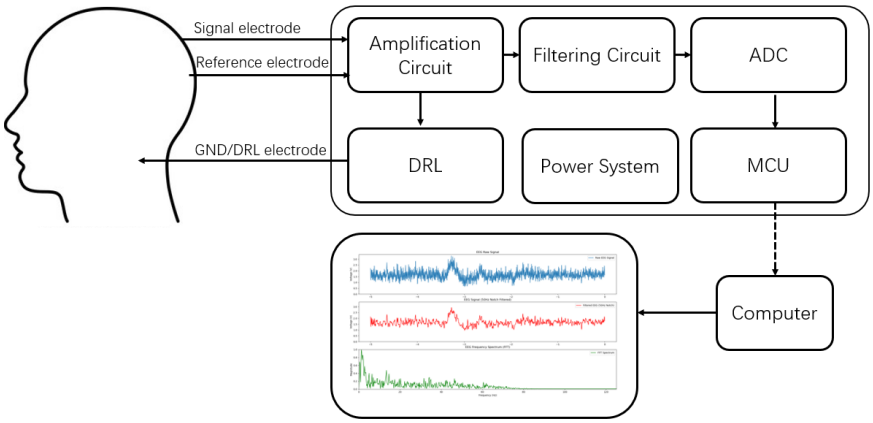

Figure 3.1: The box diagram of the entire device design.The visualization of signal includes raw data (blue), data after filtering (red) and result of FFT (green).

The signals from the four channels are fed into the four inputs of the ADC (ADS1115, TI), which continuously convert data at 250 Hz (100Hz in four channels) and communicates with the Microcontroller Unit (MCU) via the I^2C protocol. The MCU used in this device is an ESP32 series (ESP32-WROOM-32D, Espressif) chip, which includes an integrated Bluetooth module and a printed antenna. The device operates in two different modes depending on the power source. When powered via USB or other stable power source, the MCU utilizes classic Bluetooth for real-time communication with a computer, ensuring accurate data transmission. In this mode, power consumption is optimized by disabling unnecessary components such as WiFi and the internal ADC. When powered by a battery, the device switches to a long-term continuous monitoring mode, where the MCU operates in sleep mode and transmits EEG data intermittently via Bluetooth Low Energy (BLE) module.

Once the signals are transmitted wirelessly to a computer, a Python script receives and records the data from the corresponding Bluetooth port. The script also provides real-time visualization and includes essential signal processing techniques such as a 50 Hz notch filter, 70 Hz low pass filter and Fast Fourier Transform (FFT) for EEG data analysis.

fig. 3.2 and fig. 3.3 present the schematic design of the entire device in KiCad, highlighting additional details of the MCU and power system. The first figure outlines the amplification and filtering circuits as described earlier. The second figure focuses on the MCU and power management to meet the specific requirements of the device. Only essential MCU pins are reserved, including power and programming pins (3.7V, GND, EN, IO0, TXD0, RXD0), as well as I^2C communication pins. The device employs GPIO 32 and GPIO 33 for I^2C communication instead of the default ESP32 configuration (GPIO 21 and GPIO 22) because GPIO 32 and GPIO 33 can also function as RTC_GPIO during deep sleep mode. This allows uninterrupted I^2C communication in both working mode and deep sleep modes using the same two wires. The script is uploaded via USB-C through a CH340C USB-to-serial UART converter. Additionally, NMOS transistors at the EN and IO0 pins enable automatic programming mode for convenience.

The device can be powered by a single 3.7V Li-Ion battery or through a USB connection. However, different components require different power supplies:

- The amplification circuit operates on a dual power supply of ±1.5V to ±2.5V.
- The ADC requires a single supply voltage of 2V to 5.5V.
- The MCU requires a stable 3.3V input.

To meet these requirements, the power system includes a DC-DC voltage converter and a Low Dropout Regulator (LDO). The LDO (XC6206P332, UMW) convert input voltages between 1.5V and 5V to a constant 3.3V output. The DC-DC converter (LM27762, TI) provides both positive and negative outputs, which are configured using feedback resistors. In this device, the DC-DC converter is set to output ±2V.

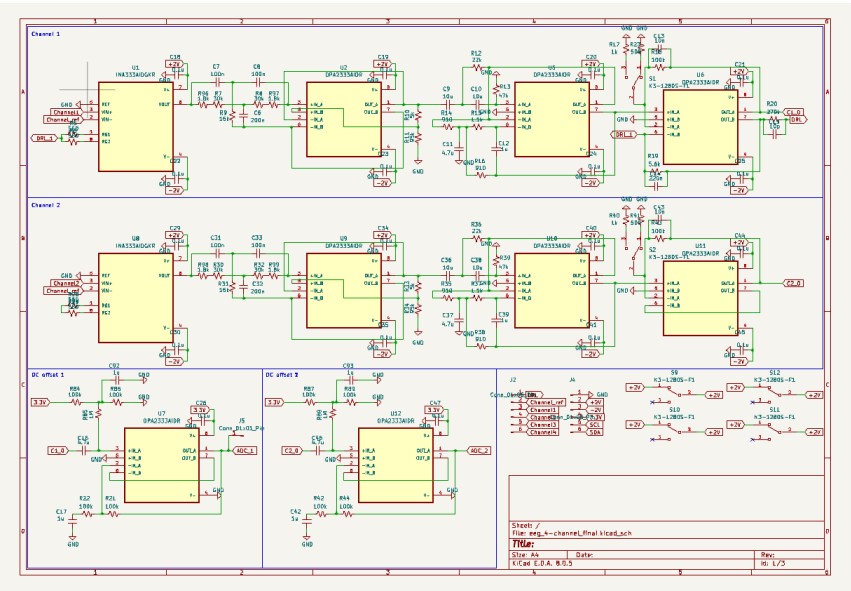

Figure 3.2: The schematic design of the amplification circuit. The third and fourth channel are not shown here but identical to the second channel.

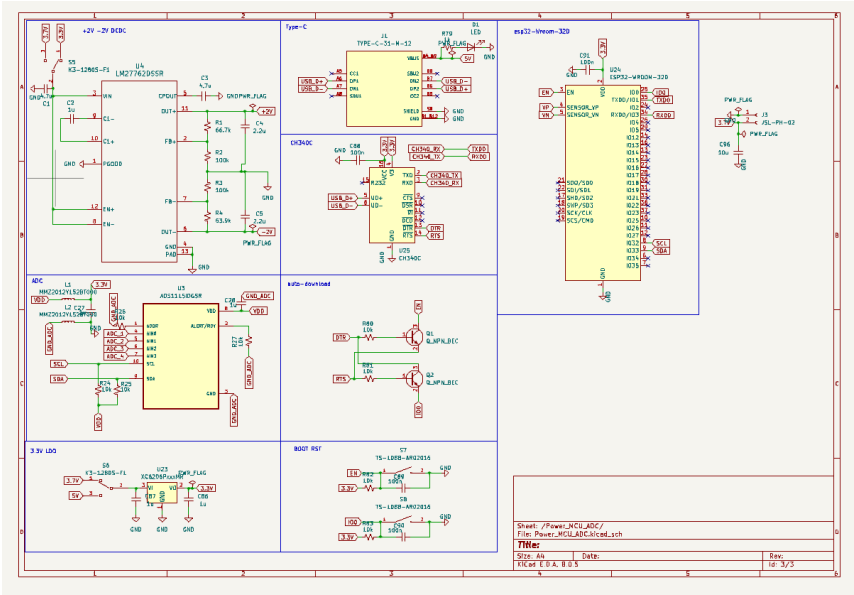

Figure 3.3: The schematic design of the MCU and power system of the device.

fig. 3.4 displays the PCB layout of the device. The overall design is compact, with separate sections for the signal processing circuit and the MCU to minimize interference from the high-frequency MCU components. The PCB includes switches to enable or disable individual channels and an adjustable gain setting for the second amplifier, allowing total gain values of 20,000 or 35,000 v/v. Additionally, an area is reserved for the battery. The device measures approximately 8 × 8 mm², making it easy to hold in hand or attach to a headband.

The PCB's output pin headers include: A 6-pin electrode connector for signal acquisition, supporting four input channels, a reference electrode, and a DRL/GND electrode. And a 6-pin header (optional during regular use) for debugging and testing power system functionality. This exposes 3.3V, ±2V outputs, GND, and I^2C communication lines (SCL and SDA) for testing.

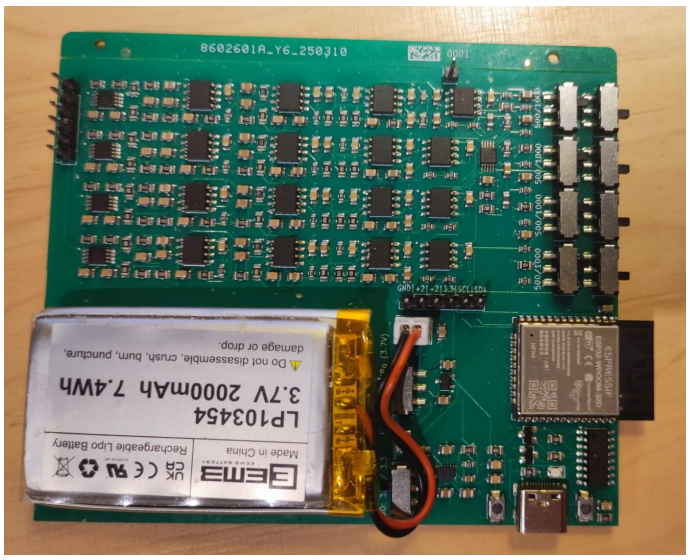

Figure 3.4: The PCB design of the device.

fig. 3.5 and fig. 3.6 illustrate the simulated amplification circuit and its frequency response. The simulation, conducted using Tina-TI with component models also from Texas Instruments, confirms the expected performance of the design. The frequency response shows that signals in the 0.5–70 Hz range are amplified by approximately 85–90 dB, consistent with second-order Butterworth filters. Additionally, the 50 Hz notch filter effectively attenuates power line interference. The DRL circuit inverts and amplifies common-mode noise with a gain of 20 before feeding it back into the body to further reduce interference.

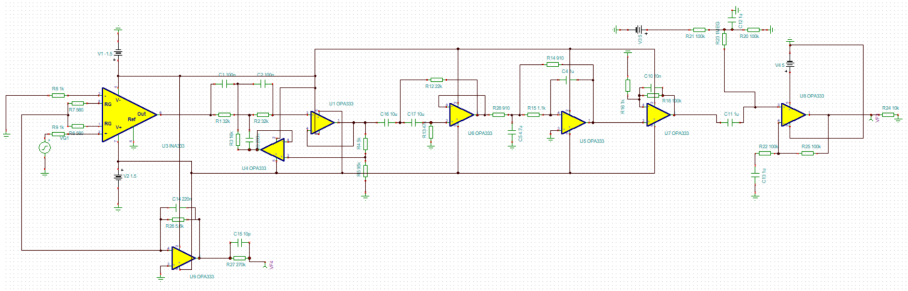

Figure 3.5: The simulation circuit of the entire device in the Tina-TI. All models have the same type with the actual components used in our device.

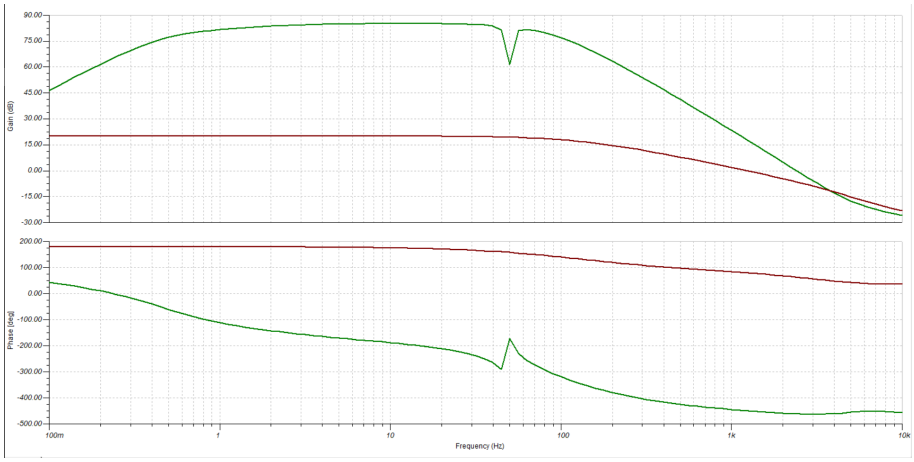

Figure 3.6: The frequency and phase response of the amplification circuit. The 0.5 to 70 Hz compoents are reserved.

4 Hardware Design

4.1 Amplification Circuit

fig. 4.1 shows that the hardware of a wearable EEG device typically includes at least three electrodes to instrumental amplifier and as GND[4], an amplification circuit, multiple filtering circuits, an Analog-to-Digital Converter (ADC) module, an MCU module for setup and wireless communication, and batteries with their relevant dependencies. The first electrode serves as the signal electrode, capturing voltage information from a specific location on the scalp. The second electrode functions as the reference electrode, providing a comparison for the signal electrode. A usable EEG signal is usually the difference between the signal and reference electrodes. For example, in the FP2-O2 montage, the collected voltage data equals $V_{FP2} - V_{O2}$, where FP2 and O2 correspond to specific placements in the standard 10–20 EEG system.

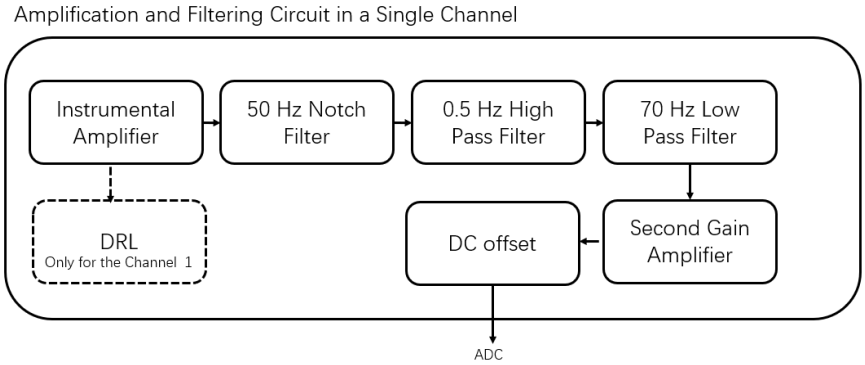

Figure 4.1: Overview of the amplification and filtering circuit. Only the first channel (Channel 1) has an additional DRL circuit. Other four channels have the identical design.

4.1.1 Instrumental Amplifier

An instrumentation amplifier (IA) is a specialized type of differential input amplifier that offers a very high common-mode rejection ratio (CMRR), high gain, and high input impedance. CMRR is defined as

$$CMRR = \frac{A_{dm}}{A_{cm}} \tag{4.1}$$

It is the ratio of differential gain and the common mode gain, A high CMRR means the effectively suppression of strong common-mode noise in EEG signals, especially 50/60 Hz powerline interference between the signal and reference electrodes[24]. For example, the INA333, an instrumentation amplifier developed by Texas Instruments (TI), has a minimum CMRR of 100 dB when the gain is greater than 10[25]. The gain of an IA typically ranges from 1 to 1000, which is sufficient to amplify biomedical signals such as ECG and EEG to an appropriate level for further amplification and signal processing. Additionally, the IA's input impedance can be as high as 100 GΩ, which is significantly higher compared to standard medical electrodes in fig. 2.4. When using a typical medical wet electrode to collect signals from the scalp, the total output impedance of the input stage is usually below 1 kΩ. This ensures the EEG signal not being completely emerging in noise.

Using an IA to amplify the differential signal between the signal and reference electrodes, rather than amplifying the signals separately and then computing the difference, is crucial.

EEG signals are very small, typically ranging from 20 to 100 µV. In contrast, noise and artifacts—such as 50/60 Hz powerline interference—can reach amplitudes as high as 100 mV. If signals were amplified separately, the EEG signal would be buried in the noise, requiring an ADC with an extremely high dynamic span and resolution. For instance, using a separate amplification circuit with a gain of 1000 would amplify the EEG signal to approximately 20–100 mV, but the noise would be amplified to 10 V, making it difficult to distinguish the true EEG signal. In contrast, using an IA with a gain of 1000 and a CMRR of 100 dB would theoretically reduce the noise to around 1 mV, significantly improving the signal-to-noise ratio (SNR) and reducing the ADC requirements.

A typical IA design is shown in fig. 4.2. It consists of three operational amplifiers (op amps). The first two act as buffer amplifiers, providing high input impedance to prevent signal loss from high-output-impedance electrodes. Additionally, the input buffer stage allows the overall IA gain to be set using a single external resistor (R3). The third op amp is a differential amplifier that rejects common-mode voltage in the two channels.

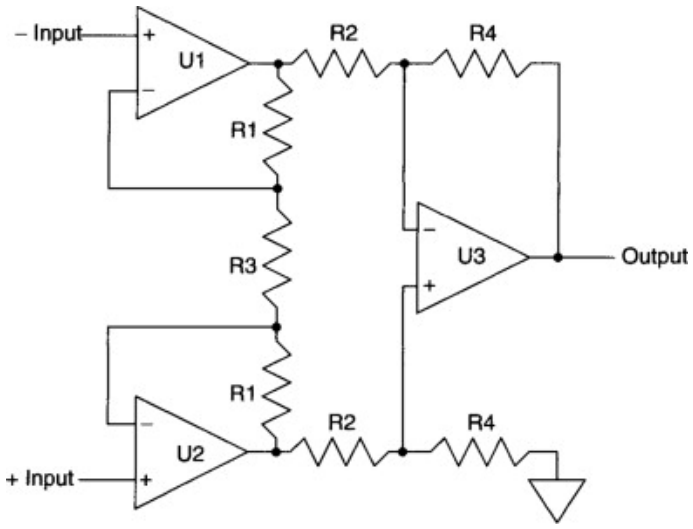

Figure 4.2: Typical schematic design of an instrumental amplifier

In detail, the input signal V_1 and V_2 can be expressed as:

$$\begin{aligned} V_{1+} &= V_{cm} + \frac{V_{diff}}{2} \\ V_{2+} &= V_{cm} - \frac{V_{diff}}{2} \end{aligned} \tag{4.2}$$

where V_{cm} represents common-mode noise and V_{diff} is the desired EEG signal. Due to the virtual short and virtual ground properties of op amps with negative feedback, the voltages at the non-inverting inputs (V_{1-} and V_{2-}) match their inverting counterparts:

$$\begin{aligned} V_{1+} = V_{1-} &= V_{cm} + \frac{V_{diff}}{2} \\ V_{2+} = V_{2+} &= V_{cm} - \frac{V_{diff}}{2} \end{aligned} \tag{4.3}$$

For V_{cm}, since $V_{1-} = V_{2-}$, no voltage drop occurs across R_3, which is often used as R_{gain}, meaning no current flows through the non-inverting input to output. Consequently, the nodal voltages at the output of U1 and U2 are V_{cm}.

For V_{diff}, R_{gain} can be modeled as two resistors, $\frac{R_{gain}}{2} + \frac{R_{gain}}{2}$, leading to a first-stage differential gain:

$$G_{diff,1} = \frac{R_1}{R_{gain}/2} \tag{4.4}$$

The second-stage op amp further amplifies the differential signal with a gain of:

$$G_{diff,2} = \frac{R_2}{R_4} \tag{4.5}$$

Typically, R_4 and R_2 are chosen to be equal for simpler calculations. Thus, the total differential gain is:

$$G_{diff} = \frac{R_2}{R_4} + \frac{R}{R_{gain}/2} = 1 + \frac{2 \times R}{R_{gain}} \tag{4.6}$$

The total output voltage at the end of the input buffer is:

$$\begin{aligned} V_{out,1} &= V_{cm} + G(\frac{V_{diff}}{2}) \\ V_{out,2} &= V_{cm} - G(\frac{V_{diff}}{2}) \end{aligned} \tag{4.7}$$

The output voltage from the input buffer is then processed by the third op amp to compute the difference:

$$V_{out} = 1 \times (V_{out,1} - V_{out,2}) + V_{ref} \tag{4.8}$$

Since typically $R_1 = R_2$, the gain remains 1. If the IA support the single-supply mode, V_{ref} is set to $\frac{V_{cc}}{2}$ instead of 0.

Finally, the IA output is:

$$V_{out} = (V_{cm} + G(\frac{V_{diff}}{2}) - V_{cm} + G(\frac{V_{diff}}{2})) + V_{ref} = G * V_{diff} + V_{ref} \tag{4.9}$$

This demonstrates that common-mode noise cancels out, leaving only the amplified differential signal. However, in practice, CMRR is not ideal due to resistor mismatches in the differential amplifier stage, preventing complete common-mode noise suppression. Integrated IA circuits such as the INA333 and AD620 typically achieve higher CMRR (>100 dB) than discrete designs using three independent op amps, with the precision-matched resistors.

Our wearable EEG device employs an INA333 with a gain of 90 v/v. According to the INA333 datasheet [25], the gain is calculated as:

$$Gain = 1 + \frac{100k}{R_{gain}} \tag{4.10}$$

Thus, two 560 Ω resistors are selected for R_{gain}, resulting in a final gain of: $1 + 100k/(2 \times 560) \approx 89.28\ v/v = 39.01\ dB$. Since the supply range of INA333 is 2.5 to 5.5 V, our device operates with a ±2 V power supply, and connect its reference pin to ground.

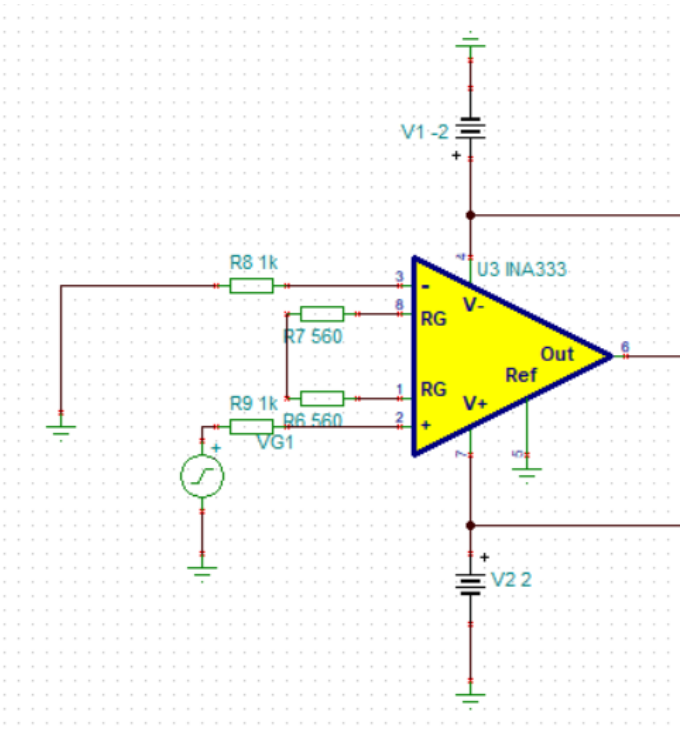

Figure 4.3: Simulate circuit of the instrumental amplifier in Tina-TI.

In fig. 4.3 and fig. 4.4, using TI's SPICE-based simulator, Tina-TI, the frequency response for the differential signal is approximately 39 dB. In contrast, the common-mode noise response in another simulation is as low as -80 dB, demonstrating effective noise suppression.

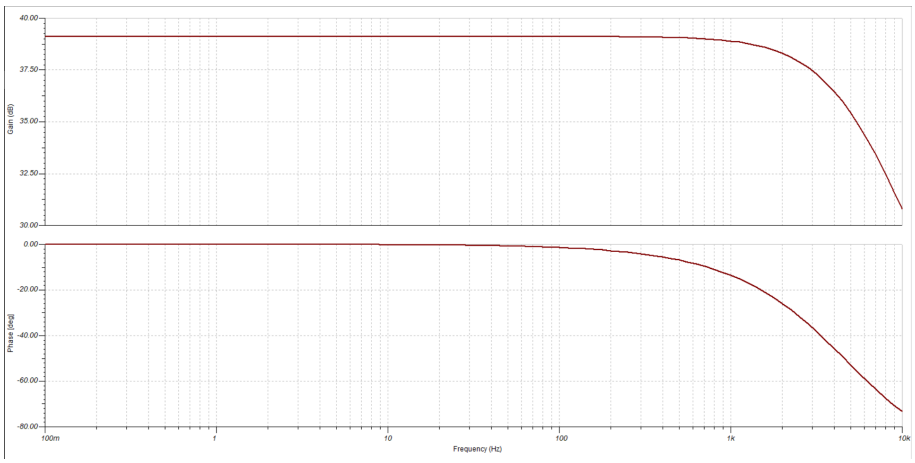

Figure 4.4: The simulated frequency response of our instrumental amplifier circuit design using Tina-TI. The first row is the amplitude response and the second row is the phase response.

4.1.2 Driven Right Leg (DRL) circuit

The Driven Right Leg (DRL) circuit is a technique commonly used in electrocardiography (ECG)[26]. Its name originates from the placement of one of the electrodes on the right leg in early versions of the circuit, though the electrode's position is no longer strictly

confined to the right leg. The primary purpose of the DRL circuit is to reduce common-mode interference by introducing an additional operational amplifier (op amp) to build the feedback to body. While the DRL circuit is typically used in ECG, some studies have demonstrated its effectiveness for EEG signal recording as well[27].

A typical DRL circuit used in ECG signal recording is shown in fig. 4.5. The first part of the circuit, which includes two op amps connected to electrodes on hands (RA and LA in 12-lead ECG placement), functions similarly to the input stage of an instrumentation amplifier. It provides gain to the differential signal (V_{diff}) while keeping the common-mode voltage (V_{cm}) at a consistent level. A voltage divider circuit is then used to process V_{cm}, which is subsequently inverted and amplified. The amplified V_{cm} is fed back into the body through the right leg, the key concept in the DRL circuit. The human body behaves as an independent capacitor, making it susceptible to common-mode noise, such as 50 Hz powerline interference. The DRL circuit sends an inverted version of this common-mode signal back into the body, which reduces the common-mode voltage and creates a feedback loop that minimizes the common-mode noise, achieving a balanced point as long as the gain of the V_{cm} is nonzero.

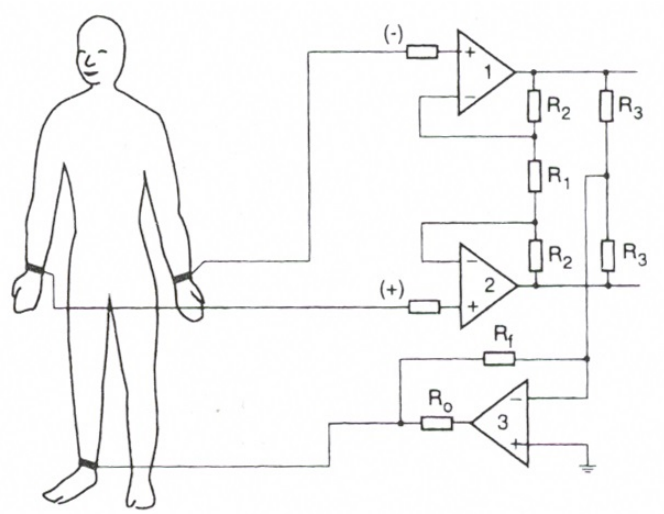

Figure 4.5: A typical circuit using DRL, the two electrodes at wrist measure the differential signal, while the electrode at ankle sends the inverted and enhanced common-mode noise back to the body.

From the induction in IA, it is clear that the output voltage of op amp 1 and op amps 2 are:

$$\begin{aligned} V_{out,1} &= V_{cm} + G(\frac{V_{diff}}{2}) \\ V_{out,1} &= V_{cm} - G(\frac{V_{diff}}{2}) \end{aligned} \tag{4.11}$$

where G is determined by resistor R_1. For V_{cm}, the voltages at $V_{out,1}$ and $V_{out,2}$ are identical, which results in two parallel resistors, and the equivalent resistance is $\frac{R_3}{2}$ for the third op amp. Thus, R_3, R_f, and op amp 3 form an inverting amplifier. Using Kirchhoff's Current Law (KCL) at the inverting input of op amp 3, we get:

$$\frac{V_{3-} - V_{DRL}}{R_f} + \frac{V_{3-} - V_{cm}}{R_3/2} + 0 = 0 \tag{4.12}$$

With the virtual ground condition of the op amps (due to negative feedback), we have $V_{3-} = V_{3+} = 0$. Therefore, the gain of the DRL circuit for V_{cm} is:

$$G_{cm} = \frac{V_{DRL}}{V_{cm}} = \frac{-2R_f}{R_3} \tag{4.13}$$

For the differential signal, since $V_{out,1} = G\left(\frac{V_{diff}}{2}\right)$ and $V_{out,2} = -G\left(\frac{V_{diff}}{2}\right)$, the voltage at the midpoint of the two R_3 resistors is zero. Thus, no differential current flows through op amp 3, and only the common-mode noise is fed back into the body.

In our device, the DRL circuit is integrated with the instrumentation amplifier (IA) circuit, as shown in fig. 4.6. Unlike traditional DRL circuits in fig. 4.5, the node introducing V_{cm} is placed at the midpoint of R_{gain}. From the perspective of V_{cm}, the voltages at the non-inverting inputs of op amp 1 and op amp 2 are both equal to V_{cm}, which achieves the same effect as the traditional design but with a more compact layout. This only requires splitting R_{gain} into two $\frac{R_{gain}}{2}$ resistors.

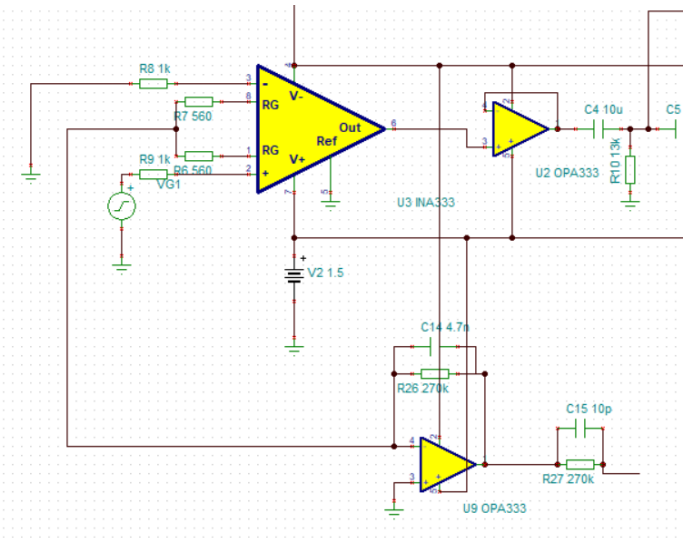

Figure 4.6: The DRL circuit integrated with IA circuit in our design. This is the simulation identical simulation circuit in Tina-TI.

fig. 4.7a shows the transient simulation of the DRL circuit with a sine wave common mode input of 100 µV amplitude at 50 Hz (red line) and DRL output (green line). The input signal varies from -100 to 100 µV. The DRL output signal has an amplitude range of approximately -110 to 70 mV, which represents an amplification of about 1000 times, and their shape is the inverse version of the input signal. fig. 4.7b illustrates the frequency response of the circuit, where all common-mode signals are amplified to 26 dB, matching the expected gain of $G_{cm} = \frac{2R_{gain}}{R_{26}} = \frac{2\times5.6\text{k}\Omega}{560} \approx 20$ v/v. The last resistor of 270 kΩ before connecting to skin is used for protection.

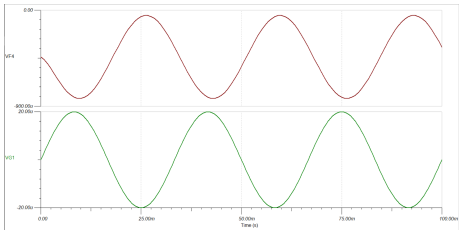

(a) The temporal simulation of the circuit with common-mode input.

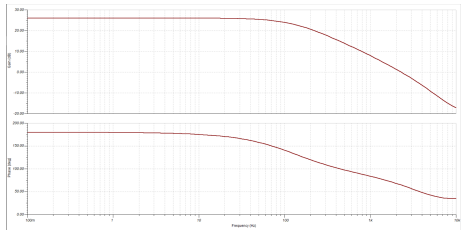

(b) Frequency response of the circuit with common-mode input.

Figure 4.7: When the input is common-mode noise.

fig. 4.8 clearly shows that the differential signal in the DRL circuit. The output is much smaller than the input signal, ideally reaching zero with perfect op amps. The frequency response also shows that all frequency components of the differential signal (V_{diff}) are suppressed.

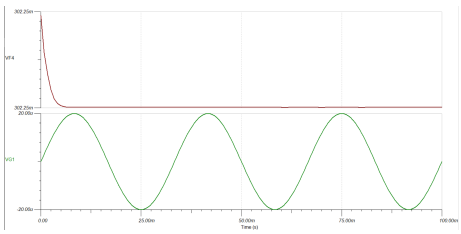

(a) The temporal simulation of the circuit with differential input.

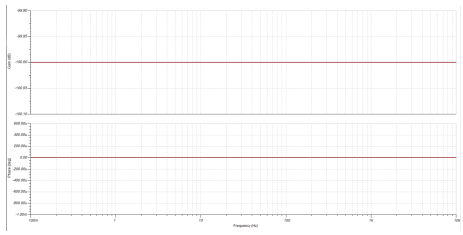

(b) Frequency response of the circuit with differential input.

Figure 4.8: When the input is differential signal.

4.1.3 Multiple stage amplification

The second amplifier is simply a non-inverting amplifier (fig. 4.9), used to further increase the EEG voltage level after the IA [28]. By applying Kirchhoff's Current Law (KCL) at the inverting input, we can derive the following equation:

$$\begin{aligned} \frac{V_{in-} - 0}{R_{16}} + \frac{V_{in-} - V_{out}}{R_{18}} &= 0 \\ \frac{V_{out}}{V_{im}} &= V_{in}(1 + \frac{R_{18}}{R_{16}}) \end{aligned} \tag{4.14}$$

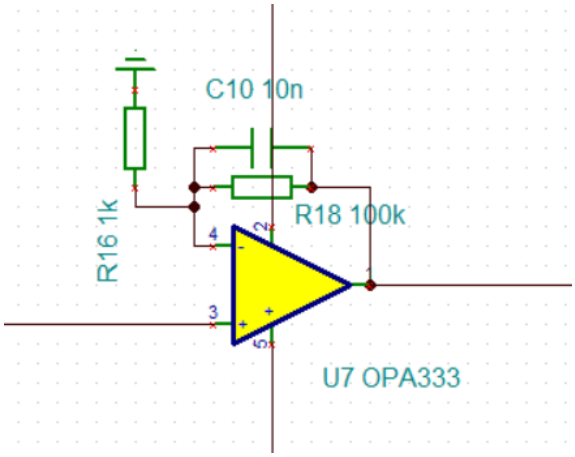

Figure 4.9: The circuit design of the non-inverting amplifier circuit.

An additional 10 nF capacitor forms a passive low-pass filter, with the cutoff frequency given by:

$$f_c = \frac{1}{2\pi RC} \approx 160Hz \tag{4.15}$$

which can further decease the influence from the high frequency noise.

Regarding the gain level of the second amplifier, the IA only provides a gain of 90 v/v, which is insufficient for EEG signals in the range of 20 to 100 µV. To bring the EEG signal to a measurable and analyzable level, we aim for a range of approximately 0.2 to 1 V. This requires a total gain of 10,000. However, if the gain is set too high, the signal may exceed the ADC's span, causing clipping of the useful part of the signal and resulting in a square wave. On the other hand, a gain that is too small may fail to utilize the full resolution of the ADC as shown in fig. 4.10. For example, in ECG, the P-wave has much smaller amplitude than the QRS complex and ST segment, yet it is a critical indicator of acute myocardial infarction [29]. Therefore, a gain of 10,000 is ideal for raising the EEG signal to an operable level. Other components can fine-tune the gain between 1 and 10 to better match the ADC's resolution and range. Thus, the second amplifier has a gain of around 100, resulting in a total gain of approximate 10,000 when combined with the IA and second amplifier.

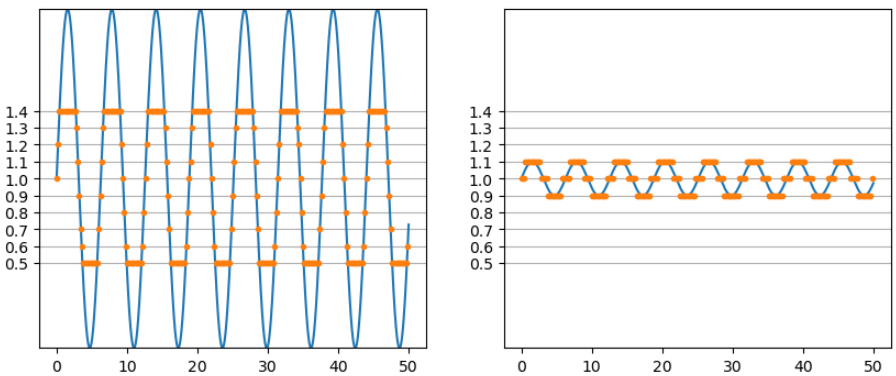

Figure 4.10: The span of the ADC. Blue line indicates signal and yellow points are samples. If the signal exceed the span, the signal will be clipped. If the signal is too small the information may not be reserved.

While the INA333 instrumentation amplifier can provide a gain of over 1000, it may be more practical to directly amplify the signal to 10,000 in a single stage to minimize noise from multiple devices. Why is the gain step of 100x100 chosen? In the previous section, the IA gain was calculated using the formula $Gain = 1 + \frac{100k,\Omega}{R_G}$. To achieve a gain of 10,000 directly, R_G would need to be set to 10 Ω, which is very small. This implies that the current flowing through the resistor would be $A = \frac{0.2 \sim 1V}{10} \approx 20 \sim 500$mA, which is too high for a low-power device. Additionally, the IA is not an ideal device, and the performance at higher gains becomes non-compliant with our requirements. According to the datasheet, the performance of the IA at a gain of 1000 is already below the required standards. As shown in the fig. 4.11, while the Common-Mode Rejection Ratio (CMRR) at a gain of 1000 is superior across all components, both gain levels (100 and 1000) perform similarly at 110 dB at 50 Hz, the main frequency of powerline noise. However, as shown in the right figure, increasing the gain reduces the frequency range that can be amplified. At a gain of 100, frequencies below 1000 Hz are amplified uniformly. At a gain of 1000, only frequencies below 100 Hz are amplified, which is insufficient for detecting important pathophysiological signals such as ripples and fast ripples.

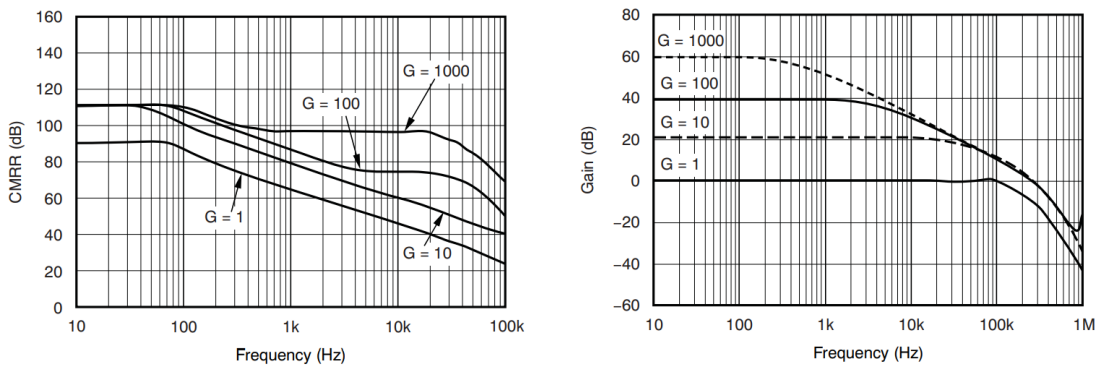

(a) CMRR Vs Frequency of INA333[25].

(b) Gain Vs Frequency of INA333[25].

Figure 4.11: Electrical characteristics from the datasheet of INA333, the instrumental amplifier type we are using.

Additionally, the total gain of the device can be easily adjusted over a wide range if using a potentiometer between R_{16} and ground. For instance, by using a 1–10kΩ potentiometer in the design, the device can be adapted for both ECG and EEG monitoring. If the gain for ECG is 1,000 and the gain for EEG is 20,000, the values of R_3 and R_4 can be calculated as:

$$\begin{aligned} \frac{R_{18}}{R_{16} + 0} &= 10 \\ \frac{R_{18}}{R_{16} + 1000} &= 200 \end{aligned} \tag{4.16}$$

When the potentiometer is set to its lowest level, the total gain will be 90 × 10 = 900, and when set to its highest level, the total gain will be 90 × 200 = 18,000. This allows for flexible gain adjustment during the design stage. Although it's possible to place the potentiometer at the R_G of the IA, the gain range for the IA is only around 100 to 1000, which isn't suitable for EEG applications.

4.2 Filtering

4.2.1 High Pass Filter

After the IA, a high-pass filter (HPF) with a cutoff frequency of 0.5 Hz is used to cancel the DC offset and reduce low-frequency noise, such as drift and motion artifacts. The choice of cutoff frequency is based on common EEG waveforms. Delta waves in EEG typically range from 0.5 to 4 Hz, so an HPF with a 0.5 Hz cutoff effectively filters out unwanted low-frequency noise while preserving useful signal components.

In this design, a second-order Sallen-Key topology is used for the HPF, as shown in fig. 4.12[30]. The Sallen-Key configuration consists of two resistors (R_1, R_2) and two capacitors (C_1, C_2), while R_3 and R_4 are not using here.

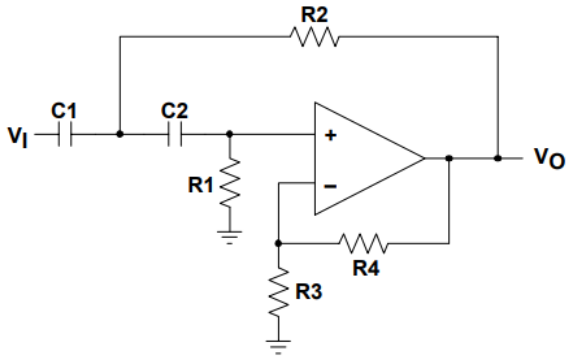

Figure 4.12: High-Pass Sallen-Key Circuit.

To get the transfer function $H(s) = \frac{V_{in}}{V_{out}}$ of circuit above, using KCL at the node A between C_1 and C_2 and node B between C_2 and R_1 will result following:

$$\frac{V_A - V_{in}}{1/sC_1} + \frac{V_A - V_B}{1/sC_2} + \frac{V_A - V_{out}}{R_2} = 0 \tag{4.17}$$

and

$$\frac{V_B - V_A}{1/sC_2} + \frac{V_B}{R_2} = 0 \tag{4.18}$$

Because of the virtual short and virtual ground properties of ideal op amp with negative feedback, the voltage at non-invert input, invert input and output are the same, that is:

$$V_B = V_{out} \tag{4.19}$$

Replace the V_B in the eq. (4.17) will return:

$$sC_1(V_A - V_{in}) + \frac{V_A - V_{out}}{R_2} + sC_2(V_A - V_{out}) = 0 \tag{4.20}$$

and eq. (4.18) is

$$sC_2(V_B - V_A) + \frac{V_B}{R_2} = 0 \tag{4.21}$$

Replace V_A in eq. (4.21) to the eq. (4.20), and all V_B to V_{out},it returns:

$$H(s) = \frac{V_{out}(s)}{V_{in}(s)} = \frac{R_1R_2C_1C_2s^2}{R_1R_2C_1C_2s^2 + (R_2C_1 + R_1C_2)s + 1} \tag{4.22}$$

Clearly Sallen-Key topology designs a second order filter, and the cut-off frequency is given:

$$f_c = \frac{1}{2\pi\sqrt{R_1 R_2 C_1 C_2}} \tag{4.23}$$

To find the suitable value of resistors and capacitors to build the 0.5 Hz HPF, C_1 and C_2 usually are selected at first, and in this device, capacitors with 10 μF are used. Because capacitors with large capacity over 10 μF on PCB board are usually aluminum electrolytic capacitor, which used more space on PCB board and are not bipolar which will cancel the negative or positive voltage information. Therefore, the bipolar ceramic capacitors with smaller SMT package are suitable for the device. However, the capacity of the C_1 and C_2 shall not be too small, since the value of R_1 and R_2 are inversely proportional to the C_1 and C_2 . Substituting $C_1 = C_2 = 10\mu F$ and $f_c = 0.5Hz$ into the equation, we can use regular resistors for R_1 and R_2:

$$\begin{aligned} R_2 &= 22k\Omega \\ R_1 &= 47k\Omega \end{aligned} \tag{4.24}$$

If values of C_1 and C_2 are too small like 0.1 μF , R_1 and R_2 will be very large, so an additional Johnson-Nyquist Noise should be considered. The voltage of this thermal noise is:

$$V_{noise} = \sqrt{4k_B \cdot T \cdot R \cdot B} \tag{4.25}$$

Where K_B is Boltzmann constant, T is temperature, R is resistance and B is bandwidth. To reduce the noise from such large resistance, using a op amp with lower bandwidth is helpful. The widely used op amp type such as LM358 has a bandwidth around 1 to 1.2 MHz, while our device utilize the op amp OPA333 has lower bandwidth at 300 kHz when tested with load capacitor with 0.1μF from the datasheet[31], which tremendous decrease the thermal noise caused by the large resistor. Here is the simulation result of the HPF:

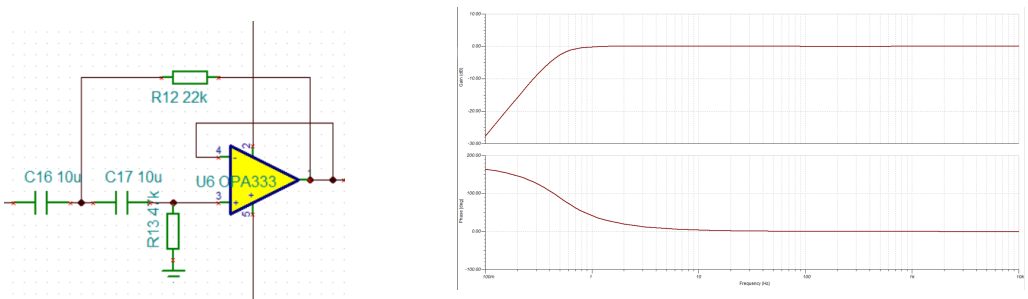

(a) The circuit design of the HPF in our device.

(b) Simulated frequency response of the 0.5 Hz high pass filter..

Figure 4.13: The simulation circuit of HPF and result.

The frequency response of the HPF shows that frequency components below 0.5 Hz are attenuated. At the cutoff frequency, the gain of the circuit is approximately -3 dB (70.7%). The filter follows a Bessel curve, ensuring no resonant peaks and smooth gain changes.

4.2.2 Low Pass Filter

After removing the DC component, a low-pass filter with a cutoff frequency of 70 Hz is employed. The cutoff frequency is chosen based on the conventional bandwidth used in clinical EEG analysis, with waveforms ranging from 0.5 Hz to 30 Hz[2]. However, in certain cases, such as epileptic foci, very high-frequency activity can occur. These high-frequency oscillations (HFOs) can be classified into gamma (30 to 80 Hz), ripples (80 to

200 Hz), and fast ripples (200 to 500 Hz). One study of subdural recordings during presurgical evaluations for epilepsy demonstrated activity bursts in a relatively lower frequency range (60 to 100 Hz) that may indicate the location of the epileptic focus[20]. Therefore, the filter bandwidth is designed from 0.5 to 70 Hz, to retain sufficient information for further signal processing and clinical analysis. This is also the recommend range from the International Federation of Clinical Neurophysiology[4].

A typical low-pass filter using multiple feedback topology consists of three resistors and two capacitors, which is different from the Sallen-Key topology by having one additional resistor, with a gain of 1[32].

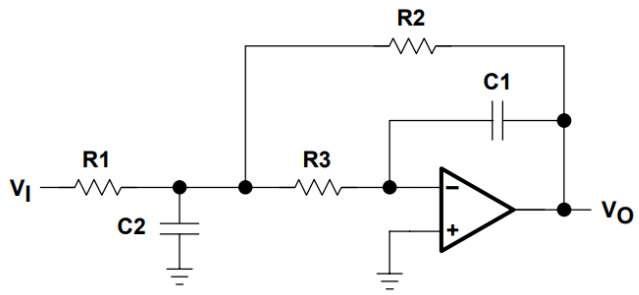

Figure 4.14: LPF.

To get the transfer function of the circuit $H(s) = \frac{V_out}{V_in}$, we use Kirchhoff's Current Law (KCL) at node A between R_1 and R_3, which gives:

$$\frac{V_A - V_{in}}{R_1} + \frac{V_A}{1/sC_2} + \frac{V_A - V_B}{R_3} + \frac{V_A - V_{out}}{R_2} = 0 \tag{4.26}$$

Next, applying KCL at node B at R_3 and C_1, we obtain:

$$\frac{V_B - V_A}{R_3} + \frac{V_B - V_{out}}{1/sC_1} = 0 \tag{4.27}$$

Due to the virtual short and virtual ground of the op amp with negative feedback ($V_- = V_+ = 0$), so there is :

$$V_B = 0 \tag{4.28}$$

Replace the V_B in eq. (4.27), it is easy to get V_A:

$$V_A = \frac{-R_3 V_{out}}{1/sC_1} = -sC_1R_3V_{out} \tag{4.29}$$

Then substitute V_A in eq. (4.29) in eq. (4.26), the relationship of V_{in} and V_{out} can be calculated:

$$\frac{sC_1R_3V_{out} + V_{in}}{R_1} + s^2C_2C_1R_3V_{out} + sC_1V_{out} - \frac{sC_1R_3V_{out} + V_{out}}{R_2} = 0 \tag{4.30}$$

From this, we can derive the transfer function:

$$H(s) = \frac{V_{out}}{V_{in}} = \frac{-1/C_2C_1R_1R_3}{s^2 + \frac{s(R_1+R_3(1+R_1/R_2))}{C_2R_1R_3} + 1/R_3R_2C_2C_1} \tag{4.31}$$

Then the cutoff frequency f_c is then given by:

$$f_c = \frac{1}{2\pi\sqrt{C_2 C_3 R_3 R_2}} \tag{4.32}$$

And the DC gain, when s equals 0, is:

$$G_{dc} = -\frac{R_2}{R_1} \tag{4.33}$$

The quality factor Q is:

$$Q = \frac{\sqrt{C_2 C_3 R_3 R_2}}{C_2(R_3 + R_2) + C_3 R_2} \tag{4.34}$$

In this design, the target is to achieve a cutoff frequency of 70 Hz, a gain of 1, and a Butterworth response to avoid ripple. The quality factor is $Q = 0.707$. Since the gain is set to 1:

$$R_2 = R_1 \tag{4.35}$$

Capacitors are typically chosen based on Q, so:

$$\begin{aligned} C_2 &= 1\mu F \\ C_3 &= 4.7\mu F \end{aligned} \tag{4.36}$$

Substituting these values into eq. (4.36) gives

$$R_1 R_3 R_2 = \frac{1}{\omega_0 C_2} \approx 2.53 \times 10^{10} \tag{4.37}$$

If R_3 and R_2 are using the same value, then $R_3 = R_1 = R_2 = 10.9k$. However, in this case, the quality factor Q does not meet the required value. To achieve Q=0.707, we adjust the values to:

$$\begin{aligned} R_1 &= R_2 = 910\Omega \\ R_3 &= 1.1k\Omega \end{aligned} \tag{4.38}$$

To save space on the PCB, the same op amp type (OPA2333) is used for both the LPF and HPF. This op amp comes in a dual package (SIOC-8).

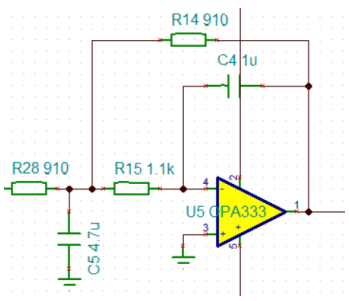

(a) The circuit design of the LPF in our device.

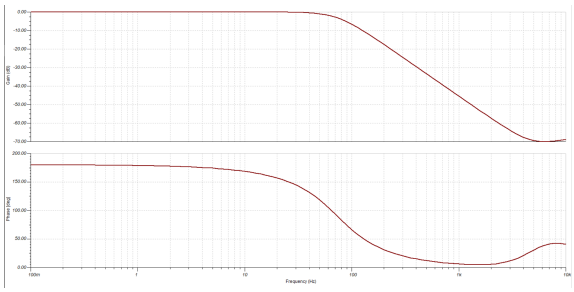

(b) Simulated frequency response of the 70 Hz low pass filter.

Figure 4.15: The simulation circuit of LPF and result.

The simulation using Tina-TI confirms that frequency components above 70 Hz are attenuated. At the cutoff frequency, the gain is approximately -3 dB, and the curve shape changes gradually, indicating a Butterworth response with $Q \approx 0.7$ which meets the design requirements perfectly.

4.2.3 50 Hz Notch Filter

Although the common-mode noise is suppressed by the instrumentation amplifier (IA), there is still significant 50 Hz powerline interference, with an amplitude around 1 mV. To further reduce this 50 Hz noise, a notch filter is necessary, which is specifically designed to address this issue.

A typical passive Twin-T notch filter consists of two symmetric circuits: one is an RC circuit, and the other is a CR circuit. These circuits are connected in parallel to form the passive notch filter. The concept behind the Twin-T notch filter is straightforward: the RC circuit acts as a passive high-pass filter (HPF), while the CR circuit acts as a low-pass filter (LPF). When both circuits have the same cutoff frequency, they provide strong attenuation at that specific frequency. The effectiveness of the notch filter depends on the depth and width of the notch, which is quantified by the Quality factor (Q). A higher Q results in a sharper notch, improving the filter's performance. However, passive Twin-T notch filters generally have a lower Q. To achieve a higher Q, the filter is often configured with two op amps to form an active Twin-T notch filter, as shown in the fig. 4.16.

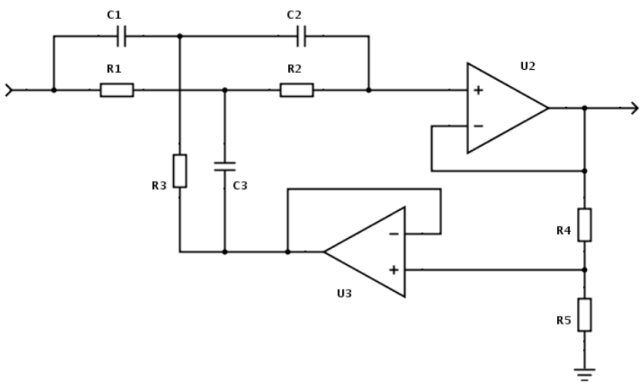

Figure 4.16: 50 Hz notch filter.

The cutoff frequencies of the two circuits are determined by the following equations, assuming $R_1 = R2$ and $C_1 = C_2$:

$$f_{LPF} = \frac{1}{2\pi R_1 C_3}$$
$$f_{HPF} = \frac{1}{2\pi R_3 C_1} \tag{4.39}$$

In a symmetric design, we set $R_3 = \frac{R_1}{2}$ and $C_3 = 2C_1$. resulting in $Q \approx 0.25$, which gives a relatively wide notch with slightly reduced filtering efficiency. To increase the Q, positive feedback is introduced via the op amp, allowing for more precise control over the notch depth and width. if Q is too small, the the notch width may include the useful frequency components like 60 Hz and 40 Hz.

The transfer function of the entire active notch filter is given by:

$$H(s) = \frac{s^2 + \omega_0^2}{s^2 + 4(1-k)\omega_0 s + \omega_0^2} \tag{4.40}$$

where $k = \frac{R_5}{R_4 + R_5}$ controls the strength of the positive feedback. The Q factor can be calculated as:

$$Q = \frac{1}{4(1-k)} \tag{4.41}$$

When k approaches 1, the Q approaches infinity. However, in practice, this can lead to oscillations due to non-ideal op amps. Therefore, a typical value for k is 0.95, which yield $Q \approx 5$.

For selecting component values, 100 nF capacitors are used, as they are commonly available and offer various advantages as discussed for the high-pass filter. To achieve a cutoff frequency of 50 Hz with $C_1 = C_2$, the resistor values are calculated as:

$$\begin{aligned} R_1 = R_2 &= \frac{1}{2\pi f_o C_1} \approx 31.83k \\ R_3 &= \frac{R_1}{2} = 15.92k \\ C_3 &= 2C_1 = 0.2\mu F \end{aligned} \tag{4.42}$$

The selection of values of R_4 and R_5 follows $k = 0.95$. Higher resistance values reduce current consumption and improve power efficiency, but excessively high values (several megaΩs) can introduce thermal noise, as discussed in the low-pass filter section. Therefore, the following values are selected to balance power consumption and signal quality:

$$\begin{aligned} R_4 &= 5k \\ R_5 &= 95k \end{aligned} \tag{4.43}$$

In our device, R_1 and R_2 are the standard 31.8 kΩ resistors, and R_3 is 16 k Ω. While it is challenging to find a single resistor with values of 31.83 kΩ and 15.92 kΩ, and connecting multiple resistors would occupy excessive space on the PCB, the resistor of 30 kΩ, 1.8kΩ and 16 kΩ are used. It should be noticed that, the selection of the 31.83 kΩ resistor influence the performance of the notch filter most, an accurate value will significantly increase the filtering effect of 50 Hz noise. This configuration results in a cutoff frequency of approximately 49.73 Hz, which is close to the target of 50 Hz.

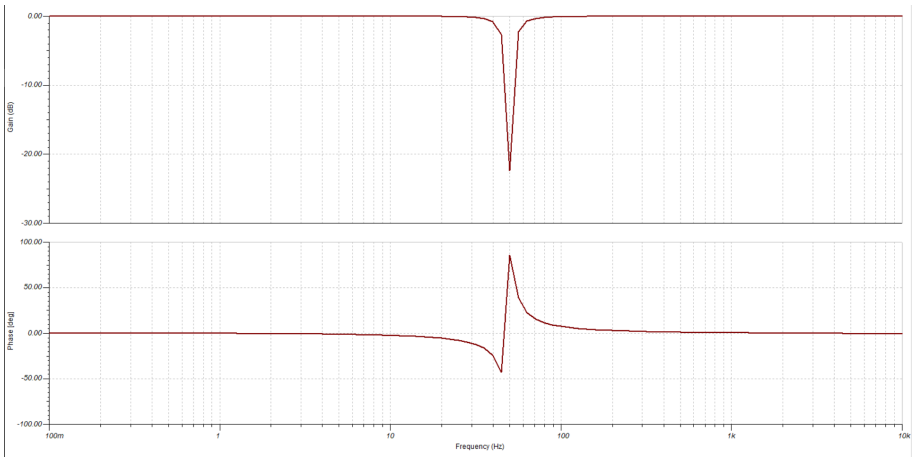

Figure 4.17: 50 Hz notch filter.

In simulation, a clear notch is observed around 50 Hz. The depth of the notch is as deep as -30 dB, indicating that the 50 Hz noise is effectively suppressed, even after the 100 dB CMRR provided by the IA.

4.2.4 DC offset

Finally, before the analog signal is sent to the ADC, the signal should be pulled up to a level higher than 0. This is necessary because the IA and op amps used in the filter circuit are powered with a dual supply of 2V and -2V. As a result, the EEG signal after amplification still has a negative component. However, most ADCs are single-supply devices, where the input range is from 0 to VCC. If the ADC is directly connected to the output of the second amplifier, the negative part of the signal will be lost, which is crucial for the EEG signal. Therefore, a DC offset circuit is needed to make the signal compatible with the ADC input.

This requirement differs from some ECG devices, which do not need a DC offset circuit, even though both ECG and EEG devices measure differential biological signals from the human body. In ECG measurements, the signal electrode is typically placed on the chest, and the reference electrode is placed at the ankle. In addition to the ECG signal, there is a constant DC voltage difference between the chest and ankle, typically around 1.5 mV. After typical amplification (e.g., a gain of 1000), the 1.5 mV ECG signal baseline becomes 1.5V, providing a natural DC offset that is sufficient to record the QRS wave in the negative domain.

However, EEG is different because the placement of the EEG electrodes does not introduce a significant DC offset[33]. The reference electrode is usually placed at Cz or Fpz, while the signal electrode is placed at other locations on the scalp. Due to their close distance, no clear DC offset is generated, meaning the EEG signal typically lies around 0V. It is important to preserve the negative component of the EEG signal in both the amplification and ADC stages.

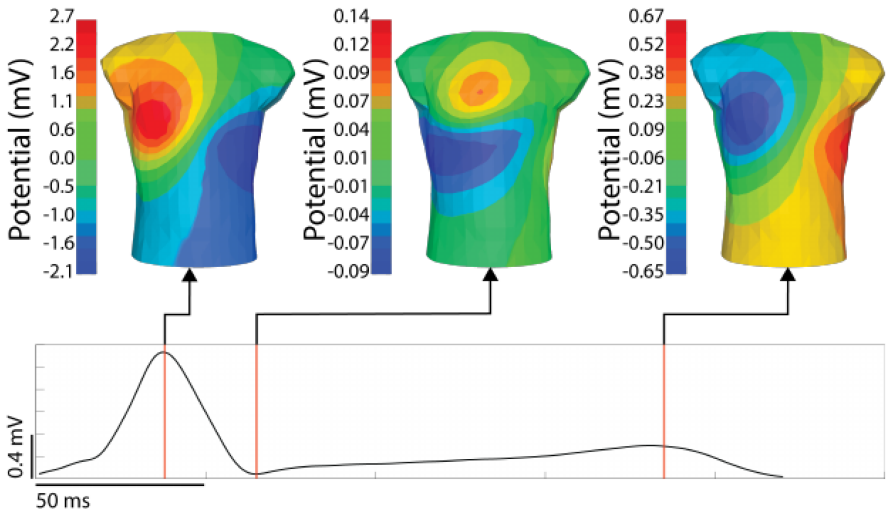

Figure 4.18: The voltage map of the chest. The voltage at chest is 20 mV highter than other places in ECG[33], while EEG does not have this DC voltage difference between signal and reference electrode.

The circuit below shows a voltage divider and an op amp-based adder. The first part generates the VCC/2 voltage, which is achieved by using two equal resistors and selecting the midpoint to obtain the VCC/2 voltage. The resistor values are chosen based on the following rule: resistors that are too large will introduce significant thermal noise by eq. (4.25), while resistors that are too small will increase current flow, leading to higher energy consumption. Therefore, a resistor value of 100 kΩ is suitable for this device.

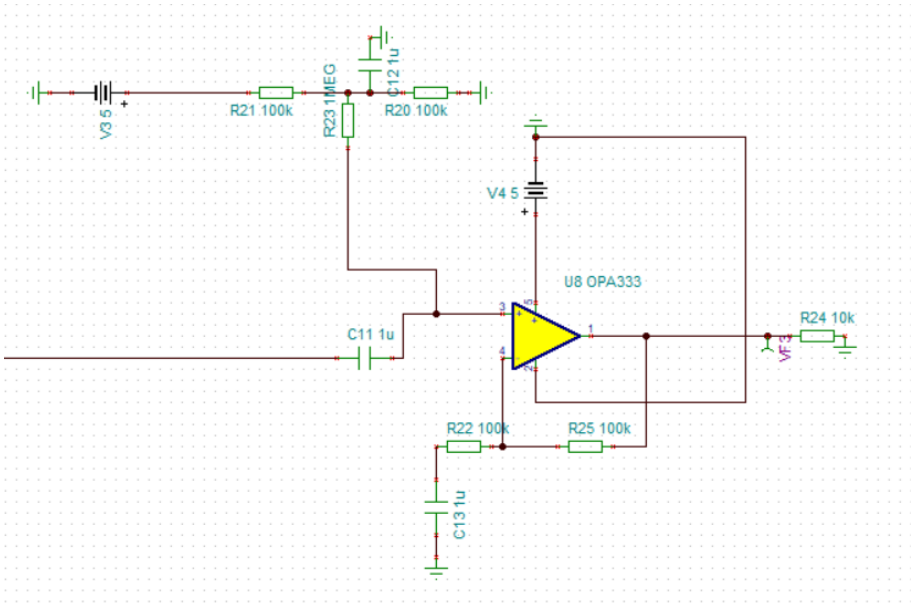

Figure 4.19: The circuit for the DC offset, including a voltage divider to provide 2/VDD and a adder circuit..

To reduce the noise from the VCC/2 source, a bypass capacitor is recommended. However, if the bypass capacitor is placed directly between the midpoint and ground, it would short-circuit the target AC signal to ground. Thus, an additional resistor is needed to prevent the signal from flowing to ground. The value of this resistor should match the input impedance of the subsequent op amp. Since the input impedance of the OPA2333 is very high (ranging from 1 MΩ to 10 TΩ), a 1 MΩ resistor can be used to form a high-pass filter with a 4.7 µF capacitor. The resulting cutoff frequency is $\frac{1}{2\pi RC} = 0.03Hz$. This cutoff frequency is low enough not to significantly affect the EEG signal.

In the adder circuit, two 100 kΩ resistors are used to build the amplifier for AC signal. The capacitor between R_4 blocks the DC voltage and build the high pass filter with 1 MΩ resistor at cut off frequency of 0.2 Hz. So, in terms of DC voltage, it behaves as a buffer amplifier with a gain of 1. However, in terms of AC signals, it functions as an amplifier with a gain of 2.

4.3 ADC

An Analog-to-Digital Converter (ADC) is a device that converts an analog signal into a digital signal. It is essential for our device because the signal, after amplification and filtering by the circuit, remains an analog continuous signal. To process the signal on a computer, it must be stored in digital form, i.e., as 0 and 1. In the fig. 4.20, the amplitude of the signal is divided into fixed values, or steps, each with the same interval. There are different methods to convert values outside the steps to the nearest one, such as using floor or ceil functions or through the circuitry inside the ADC, but these typically do not have much effect. It is clear that the smaller the height of the steps, the more accurately the ADC can preserve data from the raw signal. The number of discrete values available is called the resolution, and it is commonly expressed as the audio bit depth. For example, a 10-bit resolution ADC can convert an analog signal into $2^{10} = 1024$ different levels. The resolution in volts can be calculated based on the overall voltage measurement range. For instance, the least voltage change that can trigger a 10-bit ADC with a 5V voltage

range is:

$$V_{LSB} = \frac{E_{span}}{2^Q - 1} = \frac{5\ V}{1024 - 1} \approx 4.89\ mV/bit \tag{4.44}$$

Where LSB stands for the least significant bit, Q is the ADC's resolution, and E_{span} indicates the full-scale voltage range, i.e., the difference between the highest and lowest voltage that can be encoded. In Chapter 1, the EEG signal level is around 20 to 100 µV, which is too small to be directly recorded by a common ADC. After amplification in the previous section, the signal level becomes 20,000 times higher, around 0.4 to 2 V, making it suitable for the ADC described above. Typically, a higher resolution provides better performance, but excessively high resolution does not significantly improve the signal quality and can waste energy. Some studies have observed that a 10-bit ADC can capture useful information from AC amplified EEG signal [34].

gain errors.

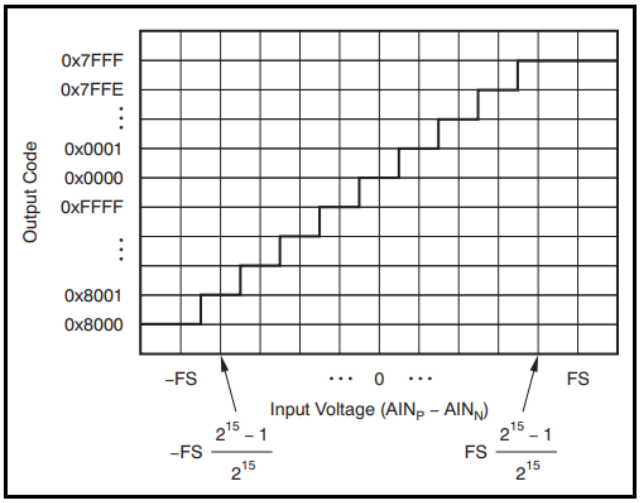

Figure 4.20: Transformation of of analog signal into a 16 bit resolution digital signal. The first bit is use to indicate postive or negative here.

In this device, the ADS1115 (Texas Instruments) with 16-bit resolution is used[35]. The ADS1115 is a small, low-power ADC with 4 channels. In continuous mode (where voltage is transformed automatically at a fixed frequency), the current consumption is only 150 µA, which is ideal for long-term monitoring. Although the international 10/20 system uses over 20 channels, not all of them are necessary. For research or experiments focused on specific areas under the scalp, fewer electrodes can still provide excellent performance. For example, some reserachers successfully classified depression at over 99% accuracy in sleep EEG using only four channels[18].

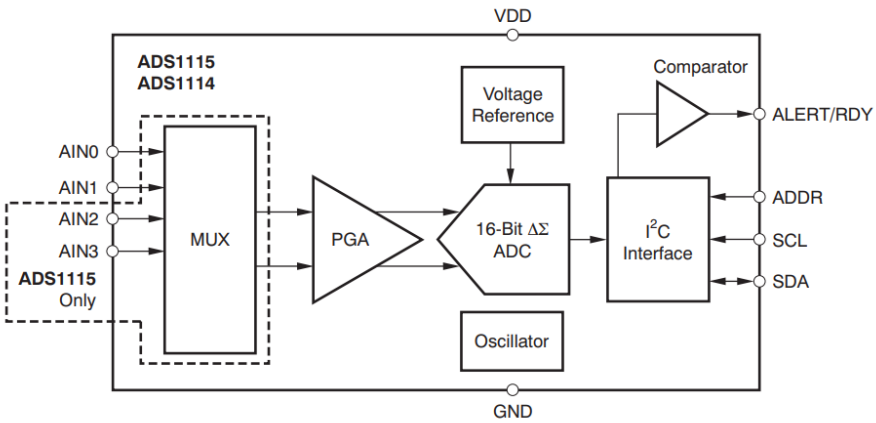

Figure 4.21: Box diagram of ADS1115[35]. MUX is in charge of the current converted channel. PGA is a programmable gain amplifier.

The supply range of 2.0V to 5.5V works well with common batteries used in wearable devices, such as 3.7V Li-Po batteries or 3V alkaline batteries. However, it should be noted that the ADS1115 is a single-supply ADC, meaning its span is from positive 2 to 5V. Since the intended EEG signal has alternating current (AC) components, directly connecting the ADS1115 to the amplification circuit will result in the loss of the negative part of the signal. There are three ways to solve this issue. The first method is to add an inverting op amp and connect the inverted signal to another channel. After manual merging in the computer, the complete signal can be preserved. The second method is to use the differential function provided by the ADS1115. This function automatically calculates the difference between two channels and saves the result. In this case, calculating the difference between the target AC signal and a suitable DC voltage (e.g., half of VCC) can also provide the complete EEG signal. However, both of these methods use two channels. The third method is to use the DC offset circuit introduced in the previous section.

In addition to resolution and span, another important parameter is the sample frequency of the ADC. In Chapter 1, commercial EEG products in hospitals usually have sample frequencies ranging from 5000 to 16000 Hz. According to the Nyquist theorem, a signal sampled at a rate F can be fully reconstructed if it contains only frequency components below half that sampling frequency ($F/2$). In Chapter 1, Section 2, the useful frequency components in EEG are around 0.5 to 70 Hz, with some special cases, such as epilepsy, where the EEG frequency can reach up to 100 Hz. Therefore, to capture these useful components in EEG, a minimum sample frequency of 140 Hz is necessary, and 100 Hz covers most normal EEG signal, with 250 Hz being better for pathophysiological conditions. The ADS1115 can provide sampling rates from 8 to 860 SPS (samples per second), which is sufficient for EEG signal acquisition. In this device, the final sample frequency is set to 250 Hz as recommended by the International Federation of Clinical Neurophysiology[4]. For the multiple channel condition, the sample rate for each channel is decrease to 100 Hz to ensure the performance of ADS1115.

4.3.1 ADS1115 setup

To use the ADS1115 for EEG signal recording, the first step is to set its mode in the config register. The ADS1115 has 5 registers, but only 3 are used (one pointer register, conversion register and configuration register in fig. 4.22). The config register contains 16 bits, each defining how the ADS1115 operates. For example, the 4th bit, called MODE,

is set to 0 for single conversion (the ADC converts data once and stops) and to 1 for continuous conversion at a frequency defined by bits 12-14. The intended mode for this device is to perform continuous conversions at 250 Hz. Therefore, the value written to the config register is 0xC3, where the prefix 0x indicates the value is in hexadecimal. The details of writing, reading and communication will be discussed in Chapter 5 and 6.

Table 7. Pointer Register Byte (Write-Only)

BIT 7	BIT 6	BIT 5	BIT 4	BIT 3	BIT 2	BIT 1	BIT 0
0	0	0	0	0	0	Register address	

Table 8. Conversion Register (Read-Only)

BIT	15	14	13	12	11	10	9	8	7	6	5	4	3	2	1	0
NAME	D15	D14	D13	D12	D11	D10	D9	D8	D7	D6	D5	D4	D3	D2	D1	D0

Table 9. Config Register (Read/Write)

BIT	15	14	13	12	11	10	9	8
NAME	OS	MUX2	MUX1	MUX0	PGA2	PGA1	PGA0	MODE
BIT	7	6	5	4	3	2	1	0
NAME	DR2	DR1	DR0	COMP_MODE	COMP_POL	COMP_LAT	COMP_QUE1	COMP_QUE0

Default = 8583h

Figure 4.22: The register used in the communication with ADS1115. Point register defines the current operating register. Conversion register stores the latest 16-bit result. Config register define which channel to and how to work.

4.4 Power Management

As mentioned earlier, the amplification circuit requires a dual power supply, while the ADC supports only a single power supply mode. Additionally, the MCU, which will be integrated later, also requires a stable power supply. In a wearable device, the size and capacity of the battery are highly constrained. To achieve longer battery life, larger capacity are required; however, the dual power supply setup demands two identical power sources. Moreover, each component's supply voltage range impacts the power system configuration.

From the datasheet, the recommended supply range for the INA333 is 1.8V to 5.5V, and for the OPA2333 operational amplifier, it is also 1.8V to 5.5V. In a dual power supply configuration, the voltage range is ±0.9V to ±2.75V. The ADS1115 ADC requires a supply voltage of 2V to 5.5V. For the MCU, a stable 3.3V supply is necessary.

For the power source, several battery types were tried and considered. Two 1.5 V AA alkaline batteries can power the amplification circuit but are insufficient for the MCU, and their size is too large for a wearable device. Two 3V CR2032 batteries, although compact, exceed the voltage limits of the OPA2333 and have much smaller capacity—about ten times smaller than alternatives. Therefore, the device will use a rechargeable 3.7V Li-ion battery as the primary power source. The required voltage levels will be generated through the components detailed below.

To generate dual voltages from the single 3.7V battery, an LM27762 module is used in this design[36]. The LM27762 is a low-noise, positive and negative output integrated charge pump with LDO (Low Dropout Regulator). It converts input voltages ranging from 2.7V to 5V into ±1.5V to ±5V. This is achieved via an inverting charge pump for the negative voltage and two LDOs for positive and negative outputs. In this design, the positive and negative 2V outputs are suitable for the IA and operational amplifiers. The voltage levels are set by the peripheral resistors.

The typical schematic for this setup is shown below:

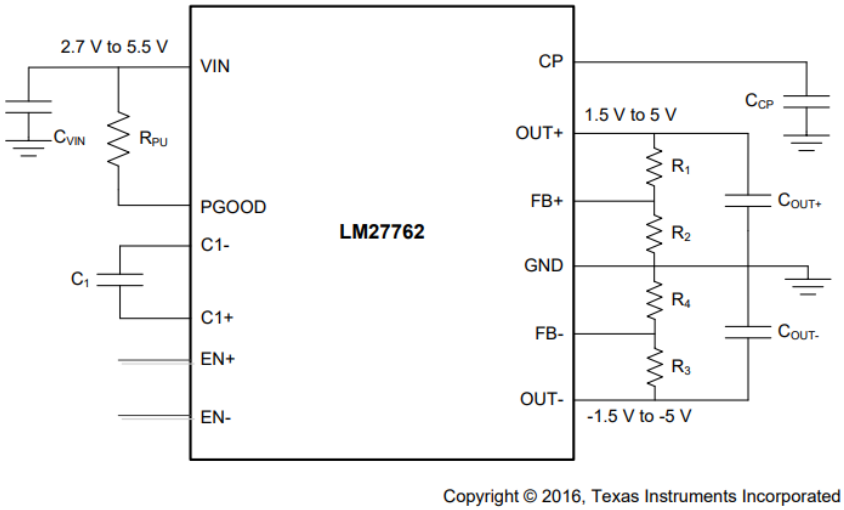

Figure 4.23: Diagram of the LM27762 from datasheet.

The output voltage is determined by the resistors connected to the OUT+ and OUT- pins, and the feedback pins (FB+ and FB-). According to the datasheet, the typical feedback voltages are $V_{FB+} = 1.2V$ and $V_{FB-} = -1.22V$. To obtain the desired positive and negative 2V at OUT+ and OUT-, the resistor values can be calculated using Kirchhoff's Current Law (KCL):

$$\begin{aligned} \frac{V_{FB+} - 0}{R_2} + \frac{V_{FB+} - V_{OUT+}}{R_1} &= 0 \\ \frac{V_{FB+} - 0}{R_2} + \frac{V_{FB+} - V_{OUT+}}{R_1} &= 0 \end{aligned} \tag{4.45}$$

By substituting the values of V_{FB+}, V_{OUT+}, and V_{OUT-}, the relationship between the resistors is:

$$R_1 = \frac{1.2 \cdot R_2}{1.3} \tag{4.46}$$

Since R_2 should not be smaller than 50kΩ[36], we use a 100kΩ resistor for R_2 and select $R_1 = 66.8k$ (the closest real value is 66kΩ). This gives an output of 1.99V and 2.01V, which suits our needs. However, this setup does not fully comply with typical 3.7V Li-Po batteries with protection circuits. Since the charge pump generates the negative voltage using a 2MHz oscillator, it may activate the protection circuit in Li-Po batteries. As such, we will use a 3.7V Li-ion battery instead.

For the MCU's 3.3V supply, the AMS1117 LDO regulator is a common choice, widely used in devices powered by 5V input (e.g., USB-C). It provides a stable 3.3V output with a current capacity of up to 1A. However, the AMS1117 does not perform well with a 3.7V input since its dropout voltage ($V_{in} - V_{out}$) must be greater than 1.5V. For stable 3.3V output, a minimum input voltage of 4.8V is required, which exceeds the 3.7V provided by the Li-ion battery.

Therefore, we use an alternative LDO, the XC6206, which is better suited to a 3.7V input[37]. The XC6206 has a lower dropout voltage (0.4V) and requires fewer peripheral components than the AMS1117, making it more compact. With a maximum output current of 200mA, the XC6206 is sufficient for our device's needs.

5 Software and MCU

5.1 MCU

The signal from the ADC is converted into 16-bit digital data, but the ADC can only store the latest conversion result. To store and transmit the current data, an embedded microcontroller unit (MCU) is needed. The MCU communicates with the ADC, stores the data in its memory, and transmits it wirelessly via WiFi or Bluetooth. The MCU should be as compact as possible to be integrated into the PCB for the wearable design. Power consumption is critical, as the MCU typically consumes the most energy. Additionally, the high-frequency noise generated by the MCU and wireless communication module could interfere with the weak EEG signal.

There are two main options for low-power, wireless communication MCUs: the nRF series from Nordic Semiconductor and the ESP32 series from Espressif. The nRF52840, part of the nRF series, is commonly used in low-power Bluetooth applications. It consumes as little as 10mA during operation but lacks a native WiFi module[38]. In contrast, the ESP32 offers support for multiple wireless protocols, including Bluetooth and WiFi. However, its power consumption is higher—around 200mA in Bluetooth operation, which is much higher than the nRF series[39].

Both the nRF and ESP32 series can be optimized to operate at lower power consumption levels. The nRF52840 can store data in RAM through the Peripheral-to-Peripheral Interconnect (PPI), while the ESP32 features an Ultra-Low-Power (ULP) core that operates in deep sleep mode when the main CPU is inactive. In their low-power modes, both devices can achieve consumption around 1mA, with the nRF series capable of even lower level(fig. 5.2). Despite its higher power consumption, the ESP32's WiFi and IoT capabilities make it more versatile for future improvements, such as the longer distance and higher stability by WiFi compared to Bluetooth. Furthermore, the ESP32 includes additional features like a temperature sensor, touch sensor, and an 8-bit DAC pin that could be useful for the impedance measurement before connecting to protect the user.

Therefore, the ESP32 is chosen for the MCU in this device.

5.1.1 ESP32

The ESP32 chip, shown in fig. 5.1, contains several key modules. The main CPU is a Dual Xtensa 32-bit LX6 microprocessor, capable of running at speeds up to 240 MHz. In addition to the main CPU, there is a co-processor called the Ultra-Low-Power (ULP) co-processor core, which is part of the Real-Time Clock (RTC) and low-power subsystem. The RTC module includes an internal clock, eight 32-bit registers, 8kB of fast SRAM, and 8kB of slow SRAM. The RTC module can be accessed by both the main CPU and the ULP, which provides significant flexibility for low-power operation.

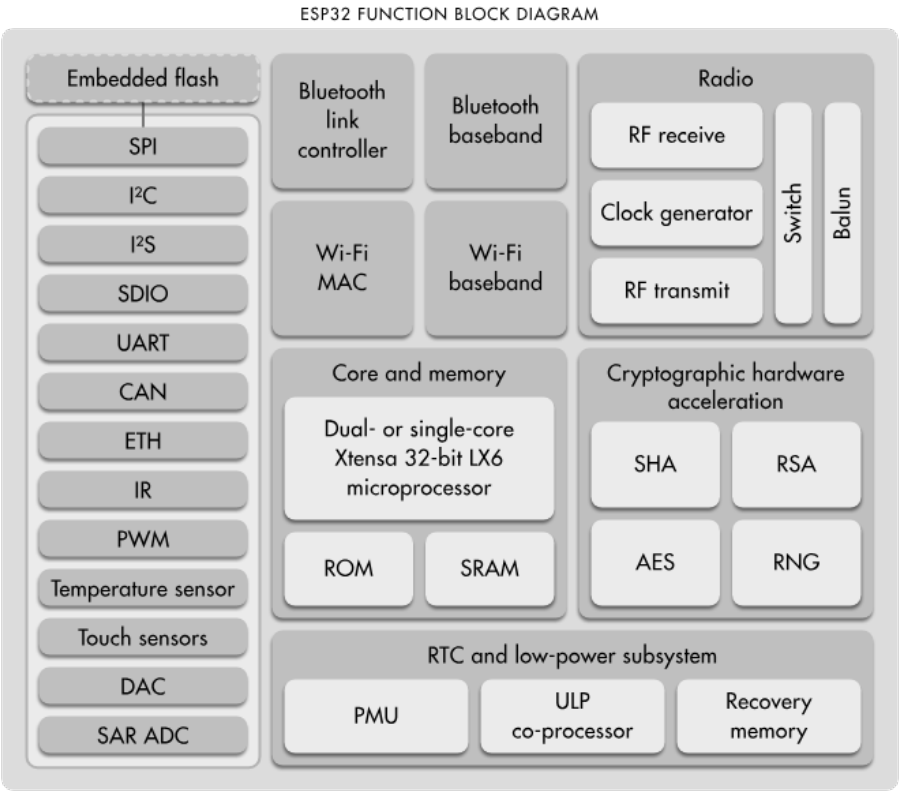

Figure 5.1: The main components of ESP32. RTC and low-power subsystem is used for optimization.

To reduce the power consumption, ESP32 provides five low-power modes for the different conditions (fig. 5.2):

- Modem-sleep
- Light-sleep
- Deep-sleep
- Hibernation
- Power off

In Modem sleep mode, the main CPU and the ULP are working in the normal speed, only unnecessary functional modules that are not declared such as DAC, sensors and WiFi will be closed, thus the power consumption could be even half of the before in the normal speed of 80 MHz. The advantage of this mode is the wireless module such as normal Bluetooth or Bluetooth Low Power (BLE) can be opened continuously by the main CPU, and the I2C communication is also operated by the main CPU. Therefore the EEG data can be monitored in realtime. In the light sleep mode, the main CPU stops work but the main memory does not clear and after the waking the data the before the light sleep can be reserved. This mode is mainly used for the discrete data recording in a fixed internal by main CPU, it stores can store the current measurement in main memory and then stops the CPU waiting for the next measurement, while the interval is controlled by the clock source in RTC. In this mode the power consumption is only around 800 μA. However the shut down of the main CPU also means that the communication with ADS1115 in high frequency through the I2C pins in main CPU is not possible, but in an Auto Light Sleep

mode, the connection of Bluetooth is kept. The third mode is Deep sleep mode. In this mode the main CPU and the main memory will stop work together, only the RTC including the ULP coprocessor are working. In RTC there is an internal 8 MHZ clock source and some GPIO pins can be used for RTC, naming RTC_GPIO. Besides, the fast RAM and low RAM are also working, in which the fast RAM mainly store the assembler code used for ULP co-processor and low RAM can be used as data storage. In deep sleep mode, the power consumption is even lower to around 200 μA. In the hibernation mode and power off mode the whole system is almost stopped and cannot do anything except waiting for the waking up by the RTC clock, thus are not usable.

Power mode	Description			Power consumption
Modem-sleep	The CPU is powered on.	240 MHz *	Dual-core chip(s)	30 mA ~ 68 mA
			Single-core chip(s)	N/A
		160 MHz *	Dual-core chip(s)	27 mA ~ 44 mA
			Single-core chip(s)	27 mA ~ 34 mA
		Normal speed: 80 MHz	Dual-core chip(s)	20 mA ~ 31 mA
			Single-core chip(s)	20 mA ~ 25 mA
Light-sleep	-			0.8 mA
Deep-sleep	The ULP coprocessor is powered on.			150 μA
	ULP sensor-monitored pattern			100 μA @1% duty
	RTC timer + RTC memory			10 μA
Hibernation	RTC timer only			5 μA
Power off	CHIP_PU is set to low level, the chip is powered off.			1 μA

Figure 5.2: The power consumption of ESP32 Series in different mode[39].

5.2 Bluetooth

To begin with, ESP32 supports two types of Bluetooth modes: Classic Bluetooth and Bluetooth Low Energy (BLE). The specific ESP32 chip used in this device is the ESP32-WROOM-32D, which supports the Bluetooth 4.2 protocol, making both Classic Bluetooth and BLE available. Classic Bluetooth is mainly used for large and continuous data transmission, such as audio and serial data transmission at very high frequencies. The transmission speed can reach up to 3 Mbps. However, not all applications require such high-speed, real-time communication, and Classic Bluetooth consumes significantly more energy even when idle. Additionally, Classic Bluetooth only supports one-to-one connections, making it unsuitable for ecosystems involving multiple devices, such as connections to a personal computer, smartphone, and smartwatch simultaneously. To address these limitations, Bluetooth SIG introduced BLE in 2010. As its name suggests, BLE is designed for low-power, intermittent data transmission, making it ideal for sensors and IoT devices.

Although Classic Bluetooth and BLE may appear similar, they operate on entirely different protocols. As a result, the modules and APIs used to program the ESP32 differ. The Classic Bluetooth protocol stack includes L2CAP (Logical Link Control and Adaptation Protocol), RFCOMM (Radio Frequency Communication), AVDTP (Audio/Video Distribution Transport Protocol), AVRCP (Audio/Video Remote Control Profile), and SDP (Service Discovery Protocol) showed in fig. 5.1.

A typical Classic Bluetooth procedure follows these steps:

1. Device Discovery: The device searches for other Bluetooth devices using the SDP module. If a response is received, containing details such as the device name, MAC address, and available services, the device pairs with the discovered device. Since

Classic Bluetooth only supports one pair at a time, it cannot connect to multiple devices simultaneously.

2. Connection Establishment: The connection is established using RFCOMM or A2DP for serial or audio data transmission. For example, when a smartphone connects to an earphone (slave), the smartphone sends a connection request to the earphone. Notably, even when no data is being transmitted, the connection remains open.

3. Data Transmission: Once the connection is established, data is transmitted using the appropriate protocol, either in streaming or packet-based mode.

4. Connection Termination: The connection is closed either manually by the user or automatically after reaching a preset maximum non-response time.

In contrast, BLE operates based on events rather than persistent connections. A typical BLE procedure follows these steps:

1. Advertising: The peripheral device (data sender) broadcasts advertisement packets on specific frequencies. These packets contain information such as the device name, UUID, and custom services.

2. Scanning: The central device (data receiver) continuously scans for advertisements. Based on the advertising packet's information (e.g., UUID), the central device can gather useful data without even establishing a connection. Since the advertisement is broadcast over specific frequencies, multiple devices can receive the data simultaneously.

3. Connection Establishment: The central device may send a connection request to the peripheral device to enable high-efficiency, continuous data transmission.

4. Data Transmission: Data is transmitted using the GATT (Generic Attribute Profile) protocol, which defines how two BLE devices exchange data bidirectionally through services and characteristics, listing 5.1 shows part of the GATT profile for our characteristics. Common predefined services and characteristics, such as heart rate and blood pressure, already have assigned UUIDs in GATT. In this device, custom services and characteristics are created for convenience.

When the device has a stable power source, such as a USB connection to a computer or power socket, Classic Bluetooth can be used for real-time EEG signal transmission. However, when the device is battery-powered and requires long-term continuous operation, or when multiple devices are used to build an EEG monitoring system with 8 to 12 channels, BLE is the preferred option.

In this device for BLE, there are two characteristics being used, the first one is the signal data, after subscribing the notification of the BLE service in ESP32, the data is encoded into a 500 byte package and sent to the computer. The second characteristic is the a controller for the working mode of the device. The computer write an uint_8 number to the device memory, then the device will change the channel numbers and sample rate based on the information.

```
// UUID for the EEG service
static const uint16_t GATTS_SERVICE_UUID_TEST       = 0x18FF;
// Characteristic 1: Signal values
static const uint16_t GATTS_CHAR_UUID_CH1           = 0x2AFE;
// Characteristic 2: Modes setting for channels and sample rate, the uuid has
    a default name "Digital Output"
static const uint16_t GATTS_CHAR_UUID_CH2           = 0x2A57;
```

```
// Declariation for Characteristic 1
// Allows to read from master and notify from the slave
[SV1_CH1_IDX_CHAR]     =
{{ESP_GATT_AUTO_RSP}, {ESP_UUID_LEN_16, (uint8_t *)&character_declaration_uuid, ESP_GATT_PERM_READ,
  sizeof(uint8_t), sizeof(uint8_t), (uint8_t *)&char_prop_read_notify}},
// Define the value of Modes: an array of uint_8 number
[SV1_CH1_IDX_CHAR_VAL] =
{{ESP_GATT_RSP_BY_APP}, {ESP_UUID_LEN_16, (uint8_t *)&GATTS_CHAR_UUID_CH1, ESP_GATT_PERM_READ,
  sizeof(sv1_char1_value), sizeof(sv1_char1_value), (uint8_t *)sv1_char1_value}},
//Description for the client
[SV1_CH1_IDX_CHAR_CFG]  =
{{ESP_GATT_AUTO_RSP}, {ESP_UUID_LEN_16, (uint8_t *)&character_client_config_uuid, ESP_GATT_PERM_READ|ESP_GATT_PERM_WRITE,
  sizeof(uint16_t), sizeof(sv1_ch1_client_cfg), (uint8_t *)sv1_ch1_client_cfg}},

// Declariation for Characteristic 2
// Allows to be read and written from master
[SV1_CH2_IDX_CHAR]      =
{{ESP_GATT_AUTO_RSP}, {ESP_UUID_LEN_16, (uint8_t *)&character_declaration_uuid, ESP_GATT_PERM_READ,
  sizeof(uint8_t), sizeof(uint8_t), (uint8_t *)&char_prop_read_write_notify}},
// Define the value of Modes: a uint_8 number
[SV1_CH2_IDX_CHAR_VAL]  =
{{ESP_GATT_RSP_BY_APP}, {ESP_UUID_LEN_16, (uint8_t *)&GATTS_CHAR_UUID_CH2, ESP_GATT_PERM_READ|ESP_GATT_PERM_WRITE,
  sizeof(sv1_char2_value), sizeof(sv1_char2_value), (uint8_t *)sv1_char2_value}},
//Description for the client
[SV1_CH2_IDX_CHAR_CFG]      =
{{ESP_GATT_AUTO_RSP}, {ESP_UUID_LEN_16, (uint8_t *)&character_client_config_uuid, ESP_GATT_PERM_READ|ESP_GATT_PERM_WRITE,
  sizeof(uint16_t), sizeof(sv1_ch2_client_cfg), (uint8_t *)&sv1_ch2_client_cfg}},
```

Listing 5.1: The defination of the service and characteristics

5.3 Python-based Visualization and Processing

After the signal is advertised by the Bluetooth module, a Python script is used to receive and process the EEG data. The data is first visualized in fig. 5.3. The first row displays the raw data received from the MCU over the last five seconds. The second row shows the signal after applying a 50 Hz digital notch filter with a Q factor of approximately 20, which helps further reduce powerline interference and a 70 Hz low pass filter to suppress unnecessary parts. The third row presents the result of the Fast Fourier Transform (FFT) applied to the filtered signal.

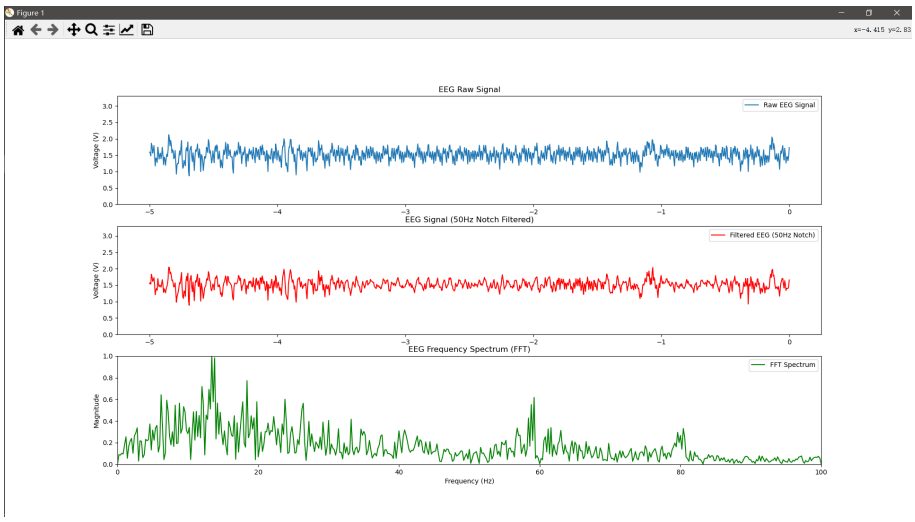

Figure 5.3: The visualization of the EEG data from the device. The visualization of signal in cludes raw data (blue), data after filtering (red) and result of FFT (green)

FFT is an algorithm that computes the Discrete Fourier Transform (DFT) of a sequence, allowing the conversion of EEG signals from the time domain to the frequency domain[40]. In the frequency domain, the EEG signal can be represented as a combination of multiple frequency components with different amplitudes (fig. 5.4). The FFT calculates the intensity of these components, which is essential for EEG data analysis. Since different EEG characteristics, such as Alpha and Beta waves, correspond to specific frequency ranges, FFT helps distinguish these components, providing insights into brain activity.

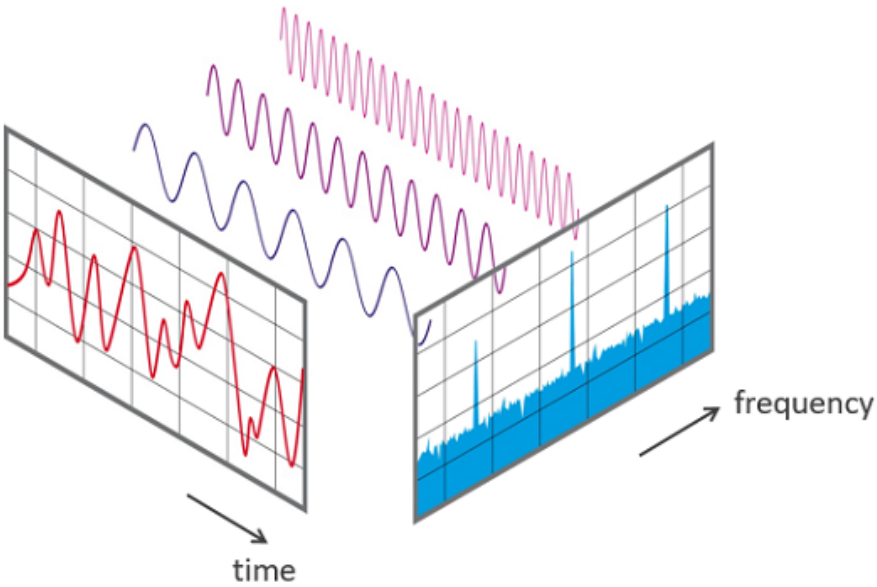

Figure 5.4: Different frequency components are stacked in the time domain.

6 Low Power Optimization

6.1 ESP32 procedure

In our device, a specialized lower power strategy is designed: the main CPU remains in deep sleep mode for most of the time, while the ULP co-processor continuously operates. The ULP co-processor communicates with the ADS1115 and wakes up at the sampling frequency to retrieve the converted data. This data is stored in RTC_SLOW_REM. Subsequently, when RTC_SLOW_MEM is full, ulp-coprocessor will wake up the main CPU to send the data through the BLE (fig. 6.1). The main CPU after waking will first initialize the BLE components and start to advertise. A relevant computer soon matches the CPU based on its device address and build the connection for notification data. After transmission, the main CPU resets the RTC storage index to free up memory for new data collection by the ULP co-processor. Finally, the main CPU returns to deep sleep mode, awaiting the next signal.

Throughout this process, power consumption remains around 5 mA, with the primary energy costs coming from intermittent main CPU operation and wireless transmission. Since the transmission time is short, the average power consumption from ESP32 is determined by the frequency of wireless communication.

Actually the main power consumption for the whole device contains: The analog circuit components including INA333, OPA2333 and ADS1115. Power Management System while XC6206 is a passive LDO and the efficient of LM27762 is around 80% and ESP32. While ESP32 uses almost 99% of energy. As a result, an optimization on ESP32 will tremendously increase the battery life of the device. We designed three modes for our device:

1. Real-time transmission with Classic Bluetooth and programmed in Arduino IDE: The current is around 200 mA, providing a similar battery life with devices introduced in table 1.2.

2. Multiple-channel intermittent transmission with BLE programmed in ESP-IDF IDE: The current is around 80 mA, archiving over 100% improvement than current device.

3. Extremely low power single-channel transmission with BLE and ULP-coprocessor programmed with assembly in ESP-IDF IDE: Most of the time the current is around 5 mA, and when transmitting data the current is 30 to 40 mA.

By optimizing these aspects, we can achieve significant power savings.

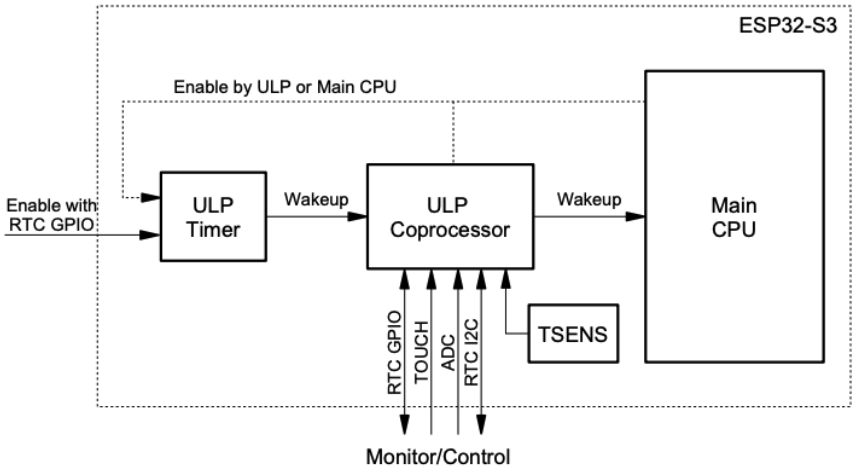

Figure 6.1: Manipulation during deep sleep. Enabling wit RTC GPIO allows the ULP-coprocessor to work with designated I^2C pins during deep sleep. The ULP timer is setting to run the ulp code in a sample frequency. The data is stored in RTC memory. When RTC memory is full, it wakes up the main CPU and main CPU starts to send data with BLE module.

Though ULP has an internal I^2C controller, the default procedure does not apply to the ADS1115 I^2C communication procedure. Therefore we need to build the I^2C in assembly from scratch. The ADS1115 is a 16-bit ADC, meaning its conversion results require 2 bytes of memory. However, due to the ULP co-processor's operating system, storing a 16-bit value requires an additional 16-bit space for command execution, resulting in each sample consuming 32 bits (4 bytes). Given an ADC sampling frequency of 250 Hz, each channel generates: $250 \times 4 = 1kB$ per seconds. With an 8 kB low memory capacity, this allows for approximately 7–8 seconds of data storage in single-channel mode and 1–2 seconds in four-channel mode, significantly reducing transmission frequency and power consumption.

6.2 I2C in Assembler

As previously mentioned, the ULP co-processor handles communication with the ADS1115. However, the ULP co-processor does not support programming in Arduino or C++ within ESP-IDF (Espressif's official development framework for ESP32). Instead, it can be programmed in assembly language. Assembly language is a low-level programming language with a strong correspondence between the instructions in the language and the architecture's machine code instruction. Since the ADS1115 communicates with the ULP co-processor using the I2C protocol over a two-wire interface, it is crucial to understand details about:

- I2C protocol
- The configuration of the ADS1115
- The architecture of the ULP co-processor
- RTC structure

By optimizing these aspects, we can achieve significant power savings.

An assembler script such as ulp.S should be integrated into the main script written in C++ as a component in ESP-IDF. After registering the ulp.S into the CMakeLists, the MCU can call the function in the ulp.S. Then the IDE will compile the application to make both the C++ script and assembly script work together. To exchange information in the RTC memory, a global parameter can be declared and used in ulp.S, while in C++ script, the parameter can also be accessed with a prefix "ulp_" at its name. For example, following code declared a parameter with a name of "count_index", the type of this parameter is a 32-bit integer with default value 0. In a more accurate way, the command indicate a space of 32-bit and the address of the first bit is pointed by a parameter with a name of "count_index". Outside the ulp.S, in C++ there is a global parameter named as "ulp_count_index". Since it is just a pointer of the address of the first bit in the whole 32-bit space, it is needed to initial the type of parameter and how to read it in the C++ scrip, such as read it in int16 format or int32 format.

```
--- ulp.S ---
.global count_index
count_index:
  .long 0
--- main.c ---
c_count_index = int32(ulp_count_index);
```

Listing 6.1: Global variable conducted in ULP-coporcessor and main CPU.

Inside the core, there are only four 32-bit registers can be used as variable called: R0, R1, R2 and R3. These four registers will be used to implement the I2C communication with ADS1115. In a typical setup, the MCU connects to the ADS1115 using two wires: SCL (clock) and SDA (data). Data is transmitted bit-by-bit using clock pulses. When SCL is high, the state of SDA determines the bit value:

- SDA = High: Represents a 1
- SDA = Low: Represents a 0

To modify the SCL and SDA levels, predefined parameters controlling the pull-up function of RTC_GPIO pins are manipulated in the code. Following codes are used to implement essential functions of I^2C, RTC_GPIO_IN_NEXT_S + 8 and RTC_GPIO_IN_NEXT_S + 9 are address for the GPIO 32 and GPIO 33. Prefix RTC means they are address in RTC so can be used when in deep sleep, where main peripheral and CPU are powered off.

```

.macro I2C_delay
  wait 10   // clock gap: 4.7us that is around 200 kHz
.endm

.macro read_SCL
  READ_RTC_REG(RTC_GPIO_IN_REG, RTC_GPIO_IN_NEXT_S + 9, 1)
.endm

.macro read_SDA
  READ_RTC_REG(RTC_GPIO_IN_REG, RTC_GPIO_IN_NEXT_S + 8, 1)
.endm

.macro set_SCL
  WRITE_RTC_REG(RTC_GPIO_ENABLE_W1TC_REG, RTC_GPIO_ENABLE_W1TC_S + 9, 1, 1)
.endm

.macro clear_SCL
  WRITE_RTC_REG(RTC_GPIO_ENABLE_W1TS_REG, RTC_GPIO_ENABLE_W1TS_S + 9, 1, 1)
```

```
.endm

.macro set_SDA
  WRITE_RTC_REG(RTC_GPIO_ENABLE_W1TC_REG, RTC_GPIO_ENABLE_W1TC_S + 8, 1, 1)
.endm

.macro clear_SDA
  WRITE_RTC_REG(RTC_GPIO_ENABLE_W1TS_REG, RTC_GPIO_ENABLE_W1TS_S + 8, 1, 1)
.endm
```

Listing 6.2: The fundamental function to pull up and down the SDA and SCL pin.

Before reading data from the ADS1115, the first step is to specify expected setting for the ADS1115. For example, in our device, it is suppose to work continuously and the SPS is 860 to fit our sample frequency. The setting up is completed by writing 16-bit value into the config register. To write the value, first the master will send a signal to start the communication. Since SCL and SDA are always in high level through a pull-up resistor, when the ULP co-processor as master decreases the level of SDA to low, while the level of SCL maintains high, it means a start signal. Then master will change the level of SCL between low and high in a fixed frequency, and the ADS1115 that is the slave can work in frequency 100 kHz or at most 3.4 MHz. In our device, 100 kHz is enough for the sample frequency of 250 Hz. If the communication is over, master will increase the level of SDA from low to high when the SCL is at high level.

Before reading data, the ADS1115 must be configured by writing a 16-bit value into its configuration register. The writing process follows these steps:

1. Start Condition: The master (ULP co-processor) pulls SDA low while keeping SCL high.

2. Send Address: The master transmits the 7-bit device address followed by a 0 (write command).

3. ACK: The slave (ADS1115) responds with an acknowledgment (SDA pulled low).

4. Send Register Pointer: The master sends an 8-bit register pointer (0x01 for the config register).

5. ACK: The slave acknowledges.

6. Send First Data Byte: The master sends the first 8 bits of the configuration value.

7. ACK: The slave acknowledges.

8. Send Second Data Byte: The master sends the remaining 8 bits of the configuration value.

9. Stop Condition: The master releases SDA high while SCL remains high.

For continuous mode operation at 860 SPS, the 8-bit configuration values are 0xC2 and 0xE3.

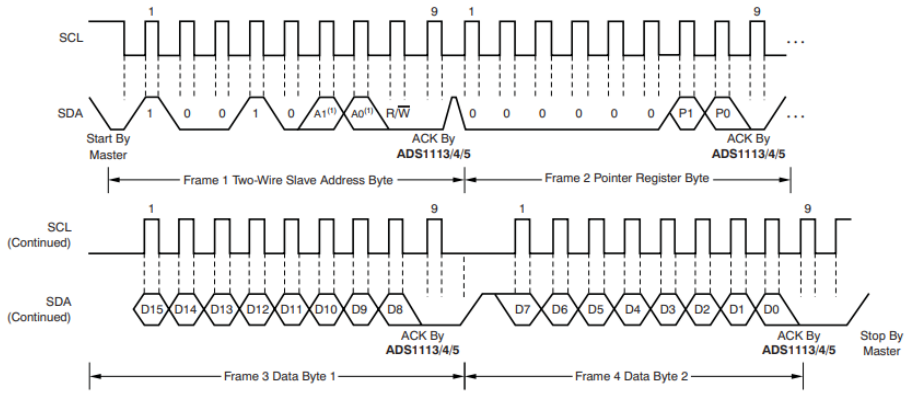

Figure 6.2: Two-wire timing diagram for write word format[35].

Reading data follows a similar sequence but requires an additional verification step:

1. Start Condition
2. Send Address with Read Command (Bit = 1)
3. ACK from Slave
4. Send Register Pointer (0x00 for conversion register)
5. ACK from Slave
6. Restart Condition (Optional Delay)
7. Receive First Data Byte
8. ACK from Master
9. Receive Second Data Byte
10. Stop Condition

The 16-bit ADC result is read in two 8-bit segments by the ULP co-processor.

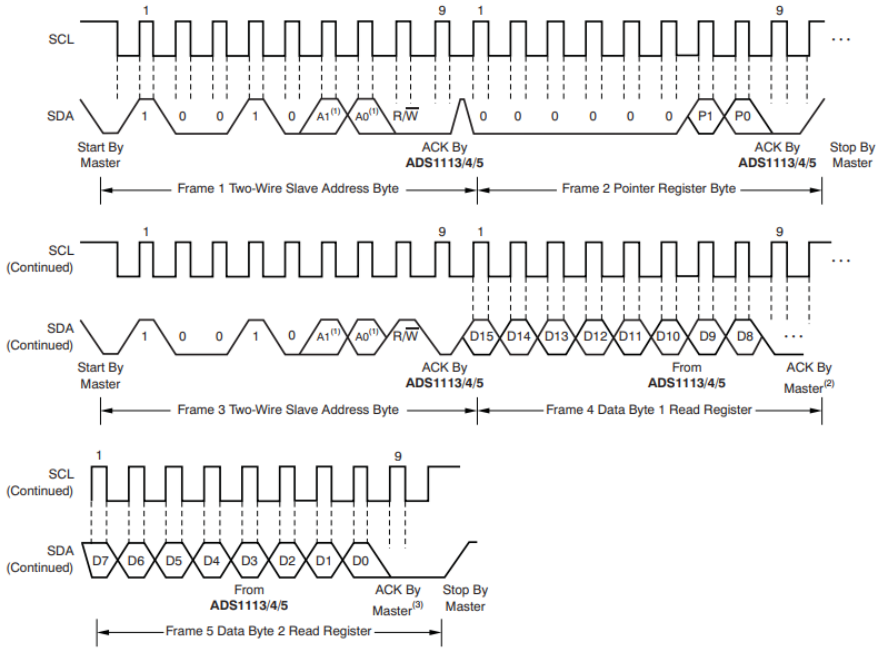

Figure 6.3: Two-wire timing diagram for read word format[35].

As mentioned earlier, ESP-IDF provides built-in I2C_WRITE and I2C_READ methods in its support library. However, these functions cannot be used directly with the ADS1115 because the official I2C write sequence does not match the ADS1115's protocol. Specifically, step 5 in the standard method includes an extra 8-bit confirmation command, which the ADS1115 does not require. And I2C_READ can reaches out single byte data, while ADS1115 reading protocol requires two bytes that is 16-bit in step 7 to 9.

In ulp.S, we first declare a parameter for the index and allocate a 4 to 7 KB space for data storage. The register R3 is used as a stack to store the address of the current command. The script consists of two main parts: the first writes a value into the configuration register, and the second stores data in the RTC slow memory.

After setup, the reading and storage operations run in a loop at a frequency of 250 Hz, which is determined based on the 8 MHz clock frequency. The running of he script is controlled by the a clock in the RTC which remains work when the main CPU is in sleep. And the I^2C communication frequency is modified by the WAIT command in assembly by indicating the cycles waiting. In this device, the communication frequency is around 200 kHz.

The ulp.S code runs continuously from device startup. In the main program, written in C++, the CPU wakes up every 17 seconds from sleep, triggered by an internal RTC clock. Upon waking, the CPU reads values from the RTC memory address previously allocated for data storage in ulp.S. Since the ULP co-processor operates with 16-bit storage, only the lower 16 bits of the 32-bit memory space are used. The collected data is then packaged and broadcast to the central device via BLE. To minimize packet loss, the advertising process repeats three times. After data transmission, the global parameter count_index is reset to zero, allowing the ULP co-processor to start recording new data. Finally, the main CPU returns to deep sleep mode and waits for the next wake-up event.

7 Experiment and result

To solve the limitation mentioned in Chapter 1. We designed three experiments to test device's performance, the influence of different electrode materials and battery life.

- Experiment 1: Testing the device under real conditions to collect usable EEG data.
- Experiment 2: Comparing different electrode materials and calculating the signal-to-noise ratio (SNR) for each type.
- Experiment 3: Measuring running current in ULP co-processor working mode and calculating battery life.

7.1 Experiment 1: EEG Signal Acquisition

In this experiment, the device functions as a single-channel EEG recorder. The first electrode is placed at Fp2 (above the eyebrow) to capture signals from the frontal lobe and eye movement artifacts. The reference electrode is positioned at O2 (occipital region), where the occipital lobe is located under the scalp. The GND/DRL electrode is placed on the earlobe. Together, these electrodes form the Fp2-O2 montage.

For this experiment, gold cup electrodes (e.g., LTC electrodes) were used, with conductive gel applied between the scalp and the electrode for improved conductivity. The EEG device is powered by a 3.7V Li-ion battery, and data is transmitted in real time via BLE. The sampling frequency is 250 Hz.

7.1.1 Stage 1: Eye movement discrimination

The experiment consists of three stages. In Stage 1, the subject wears the EEG device and performs the following actions: Blinking, Rolling eyes upward, Rolling eyes downward. The objective is to detect signals generated by eye movement. Eye movement typically produces higher voltage changes than EEG signals. If the device cannot detect these signals in real time, it may struggle to capture weaker EEG signals. The Fp2 placement is particularly susceptible to eye movement artifacts. However, relying solely on blinking may result in signals influenced by muscle contractions rather than eye movement. Therefore, rolling the eyes upward and downward is also included to differentiate eye movement artifacts from electromyographic (EMG) noise.

In fig. 7.2, eye movement artifacts originate from the charge distribution in the retina, where the front of the eye has a positive potential, and the back of the eye has a negative potential[41]. As a result, different behavior causes different EEG signals.

- Rolling eyes upward: The negative potential moves away from Fp2, causing a temporary voltage increase, which then returns to baseline. When the eyes return to their normal position, the negative potential moves closer, leading to a temporary voltage decrease.
- Rolling eyes downward: The pattern in rolling eyes upward is reversed, with a decrease followed by an increase voltage.
- Blinking: Expected to resemble the downward eye roll pattern, as blinking naturally involves a slight downward movement of the eyes.

This stage aims to discriminate eye movement artifacts from EMG noise based on these characteristic signal patterns.

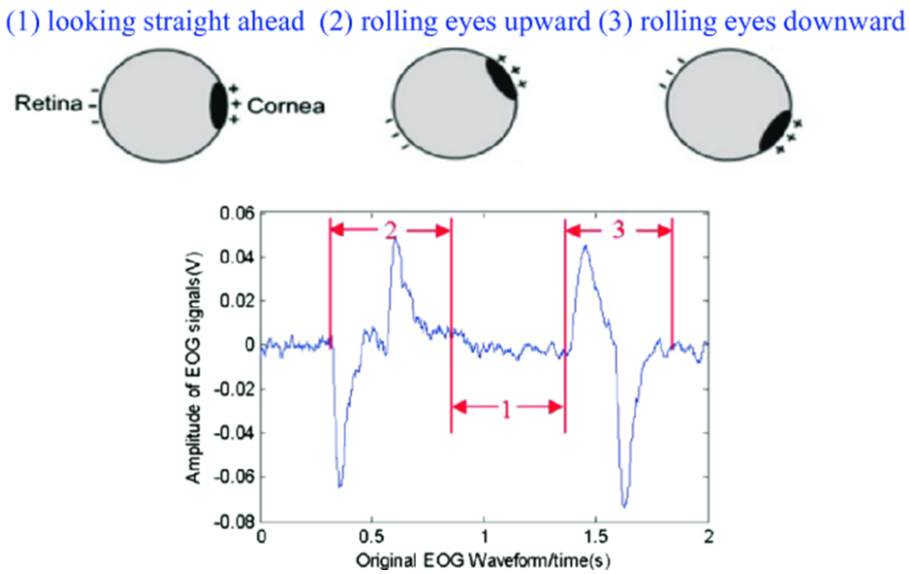

Figure 7.1: The EOG signal caused by the rolling eyeball in different direction[41].

The subject wears the EEG device and waits for signal stabilization before beginning the experiment. The subject then performs the following sequence:

BLINK, BLINK, BLINK, ROLL UP, ROLL UP, ROLL UP, ROLL DOWN, ROLL DOWN, ROLL DOWN.

Each action is repeated three times to allow comparison between samples. To minimize residual effects from the previous action, a 3-second interval is maintained between each movement. After a 10-second rest, the sequence is repeated, but with randomized order to control for sequence effects. The six different orderings help reduce bias from action placement. The total experiment duration is 3 minutes.

fig. 7.2 is the result from the first experiment in stage 1. The first row (blue lines) shows the raw EEG signal over the last 5 seconds (750 data points, given a 250 Hz sampling rate). The signal has been normalized by subtracting the mean value to remove DC offset. This normalization also improves subsequent FFT analysis. The amplitude of the raw signal ranges around 1.5 V, and the amplitude of the eye movement artifacts is as large as 2.5 V. The first artifact were generated by rolling eyeballs up, so the signal goes from low to high at first. Then with the eyeball goes back to the normal direction, the voltage changes from high to low and back to the base line. This part of the signal is captured by the electrode at the FP2 which is just above the eyes. Another reference electrode is at the head back so the it cannot receive the eye movement artifacts. The second row (red lines) shows the processed EEG signal after filtering, clearly some high frequency components has been removed from the raw data and making the result more readable. The third raw is the result of the FFT. There are three main components, the first one is the 0 to around 10 Hz alpha wave, and the second one is the 10 to 25 beta wave, both of them are common in the health people, the third one is the 50 Hz noise, the though there is a 50 Hz notch filter, there is still a lot noise around 50 Hz.

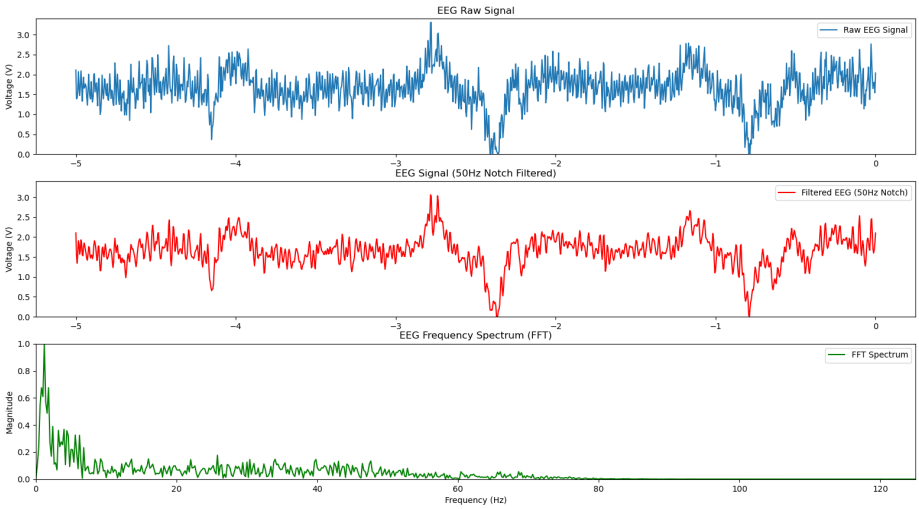

Figure 7.2: The result from the first experiment in stage 1. The first artifacts was caused by the rolling eyeballs up, and the last two artifact were caused by the rolling eyeballs down.

7.1.2 Stage 2: Enhanced Alpha wave detection

In Stage 1, the results confirmed that the collected data contained eye movement artifacts. However, this alone does not confirm the presence of high-quality EEG signals. Unlike ECG signals, which have distinct wave components such as the P wave, QRS complex, and ST-segment in the time domain, EEG signals do not exhibit easily recognizable shapes. Instead, EEG analysis often relies on frequency domain characteristics.

One well-documented phenomenon in EEG research is the presence of alpha waves (8–12 Hz) in the occipital region, particularly around the V4 area of the visual cortex. Studies have shown that when a person closes their eyes, alpha wave activity increases, reflecting a specific state of the primary visual cortex when visual input is removed. Since the O2 electrode is positioned close to the occipital lobe, it should be capable of detecting these changes. fig. 7.3 shows the pathway of the visual information received by the eye and transmitted through the visual nerves to the contralateral visual cortex that are located at the occipital lobe.

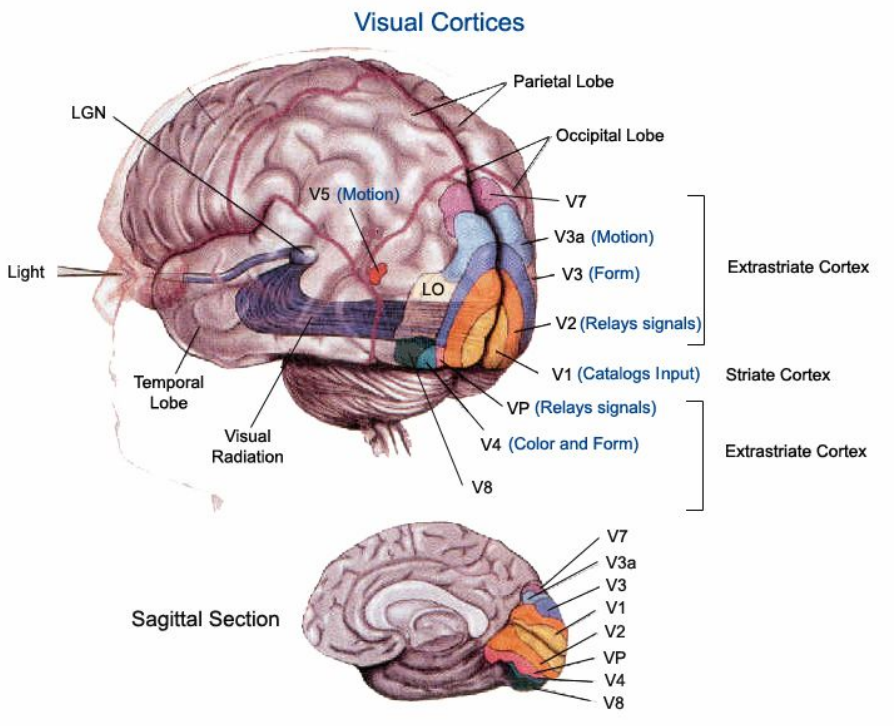

Figure 7.3: The pathway of the visual information processed in the brain[42]. The light information is receive through the eyeball and transmitted to the visual cortex at the occipital lobe.

The objective of Stage 2 is to detect alpha waves using our wearable EEG device. The experimental setup remains the same as in Stage 1, with the subject wearing the device in an Fp2-O2 configuration, as Fp2 is necessary for alpha wave detection. During the experiment, the subject performs the following actions:

CLOSEBOTH, CLOSEBOTH, CLOSEBOTH, CLOSELEFT, CLOSELEFT, CLOSELEFT, CLOSERIGHT, CLOSERIGHT, CLOSERIGHT.

Each action lasts for 20 seconds, followed by a 20-second interval. After completing the first round, the subject rests for five minutes before repeating the experiment with a different sequence of actions. The entire experiment takes approximately one hour.

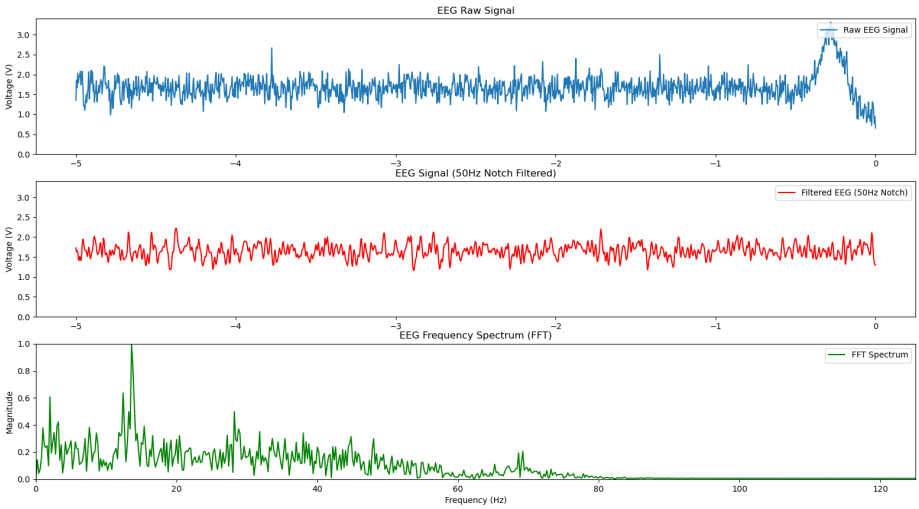

Figure 7.4: The EEG signal when eye is closed. The 12 Hz components is clearly increased.

fig. 7.4 shows the EEG signal when the eye is changed from close to open. Clearly, the signal has more lower frequency components, and after the eye movement artifact indicating the eye is opened, there are more high frequency components in the result. In the third row, the result of the FFT shows that there are more 10 to 12 Hz components in the data indicating out device successfully captured the alpah wave changes due to the eye closing in the visual cortex.

7.2 Experiment 2: Electrodes comparison

Experiment 1 demonstrated the effectiveness of our EEG device. The next step is to evaluate the performance of different electrode types. This experiment compares wet/gel electrodes, dry electrodes, and conductive polymer electrodes in terms of signal quality.

The subject repeats the Stage 2 experiment, where alpha wave activity is measured using different electrode types. The signal-to-noise ratio (SNR) is then calculated for each electrode type based on alpha wave intensity and baseline noise levels.

Here are the results comparing different electrodes. fig. 7.5 shows the EEG data recorded using wet/gel electrodes, which consist of gold cup electrodes and conductive gel. The signal quality is excellent, with an amplitude of approximately 1.5 V, and the 50 Hz powerline interference is effectively suppressed. After digital filtering, the signal becomes more readable. The FFT results also reveal the frequency components of the EEG signal.

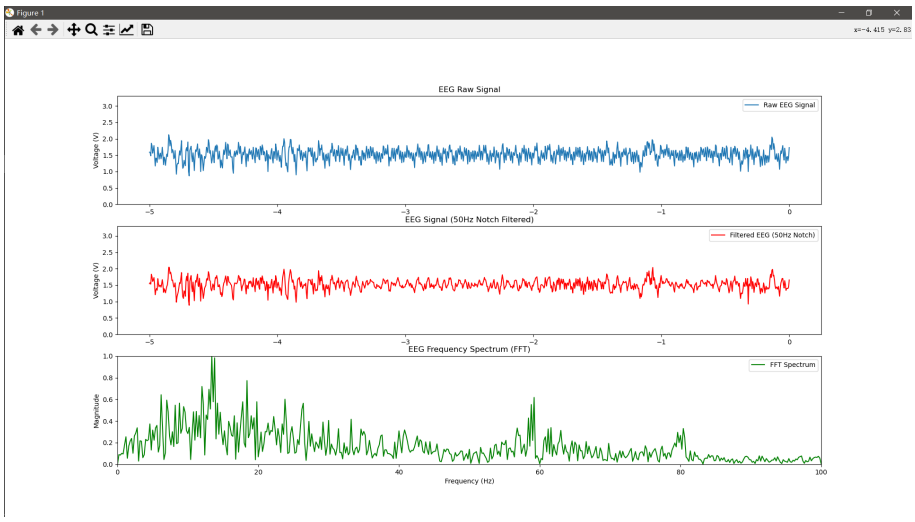

Figure 7.5: The EEG signal recorded with wet/gel electrode.

fig. 7.6 presents the EEG data recorded using dry electrodes, which in this experiment consist solely of gold cup electrodes. The first row clearly shows significantly more 50 Hz powerline interference, making it difficult to extract EEG signals from the raw data. After applying a 50 Hz notch filter, eye movement artifacts become somewhat discernible in the second row. In the third row, despite the presence of substantial 50 Hz noise components, the frequency components corresponding to alpha and beta waves remain identifiable in the FFT results.

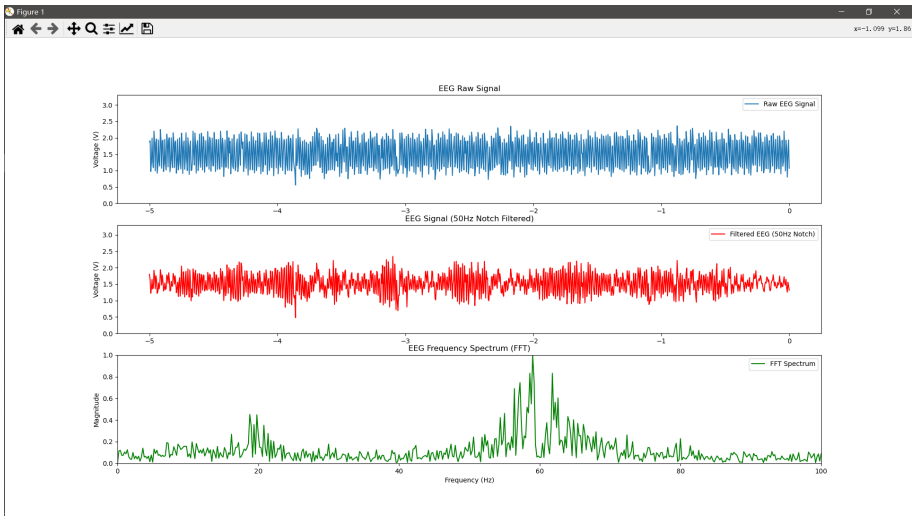

Figure 7.6: The EEG signal recorded with dry electrode.

fig. 7.7 displays the EEG signal recorded using conductive polymer electrodes. The signal is influenced by the noise, making it totally unreadable. Even after applying a 50 Hz notch filter, the signal quality remains poor. In the third row, the FFT results do not provide any useful information.

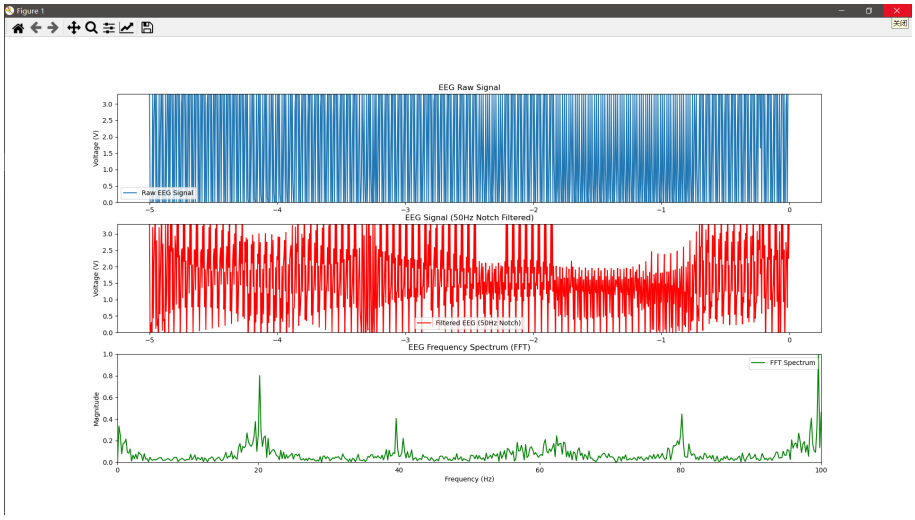

Figure 7.7: The EEG signal recorded with conductive polymer electrode.

7.3 Experiment 3: Battery life

The third experiment is to test the energy consumption of the device. Here, we recorded the current consumption from the initial setup to actual signal transmission over a period of one minute. For most of the time, the device remains in deep sleep mode. The main CPU only wakes up and transmits data through the BLE module when the RTC buffer is full. As shown in fig. 7.8, the current during deep sleep is approximately 4 to 5 mA.

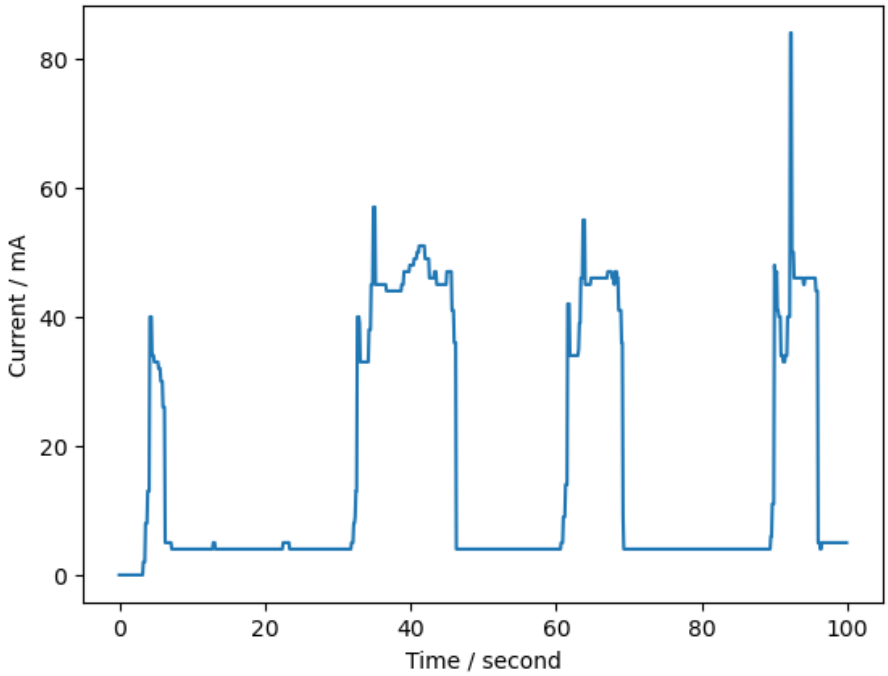

Figure 7.8: The current of the device in 1 minutes.

In the first second, when the system is powered on, the current peaks at 40 mA. Following the initialization of the ULP co-processor, the current gradually decreases as the main CPU powers down. After approximately 20 seconds, the ULP co-processor collects

enough data and wakes up the main CPU, resulting in another 40 mA peak. Shortly after stabilization, the main CPU begins advertising, causing the current to rise to 60–80 mA. However, once a connection is established with the computer, data transmission begins, and the current stabilizes at around 47 mA.

The device's average current consumption throughout the entire period is as low as 10 mA. This implies that a 2000 mAh battery could provide up to 200 hours of battery life, significantly outperforming other wearable devices listed in table 1.2.

8 Discussion

8.1 Result analysis

8.1.1 Performance of EEG Signal Acquisition

The first experiment tested the performance of the device as an EEG signal recorder. The experiment was conducted step by step.

In Stage 1, the device successfully detected eye movement artifacts, which are relatively larger than normal EEG signals. To further distinguish these artifacts from EMG signals, the experiment classified eye movement artifacts into two types: rolling the eyeballs up and rolling them down. Since eye movement artifacts originate from the electrodes near the retina, the recorded signals should differ between upward and downward eye movements. In contrast, EEG signals caused by muscle activity around the eyes should produce similar results in both cases. The recorded signals confirmed the presence of eye movement artifacts, demonstrating that the device can detect small voltage changes at the forehead.

The next step was to record real EEG signals. Unlike ECG signals, which have distinct features like the QRS wave and RT segment, EEG signals do not have clear, recognizable patterns, making them more challenging to distinguish from noise. To address this, the experiment leveraged a well-known property of EEG signals: at the back of the head, where the occipital lobe is located, EEG activity is influenced by the visual cortex. When the eyes are closed, the visual cortex processes less light information, leading to an increase in alpha wave activity in the frequency domain. Therefore, if the recorded signals showed an increase in alpha waves when the eyes were closed, it would confirm the presence of EEG signals. The experiment successfully verified this effect, confirming that the device is capable of recording EEG signals.

8.1.2 Performance of the electrode

Since the device was confirmed to record EEG data, the second experiment focused on evaluating the performance of different types of electrodes.

Wet/Gel Electrodes

The first test used wet/gel electrodes, which produced high-quality signals suitable for further analysis, such as Fast Fourier Transform (FFT). However, the experiment revealed that signal quality depended on the amount of conductive gel applied. If the gel amount was insufficient, electrode-to-skin contact was poor, leading to reduced signal quality. Additionally, wet/gel electrodes were found to be unsuitable for long-term recording, as the conductive gel dries out within 2–3 hours, requiring reapplication to maintain signal quality. Another drawback was the complexity of setup and cleanup, especially in areas with hair.

Dry Electrodes

Next, the performance of dry electrodes was tested. The results showed that 50 Hz noise significantly masked the EEG signal. However, after applying a digital 50 Hz notch filter, the EEG signal became partially distinguishable, and FFT analysis revealed characteristic EEG frequency components such as alpha and beta waves. Compared to wet/gel electrodes, dry electrodes were much easier to set up. Despite this advantage, they also had drawbacks. Without conductive gel, dry electrodes were prone to detachment, especially in areas with hair, making it difficult to maintain stable contact with the skin.

Conductive Polymer Electrodes
Finally, the experiment tested conductive polymer electrodes. However, the recorded data was unusable. The primary issue was the electrode size—approximately 2 × 4 cm²—which made it difficult to attach to areas with hair. Additionally, the conductive polymer material required a special preparation process before use. Initially, in its dry state, the material was rigid, with an extremely high impedance of 100 MΩ, making it non-conductive. After applying water and waiting for approximately 5 minutes, the material became more stretchable, self-healing, and conductive, reducing the impedance to 100 KΩ. Although the material could adhere to bare skin without additional gel or adhesive, it was still ineffective in areas with hair.

Even when tested on hair-free areas such as FP1 and FP2, the electrodes failed to produce usable data. One possible explanation is that previous impedance measurements of the material were conducted using DC voltage, while EEG signals are AC signals. The impedance behavior of the material under AC voltage remains unknown. Additionally, after preparation, the conductive polymer material gradually dried out over 5–6 hours, likely altering its electrical properties, including impedance. This suggests that, similar to wet/gel electrodes, conductive polymer electrodes may require reapplication for long-term monitoring beyond 6 hours. Further research and testing are necessary to improve the performance of conductive polymer materials as EEG electrodes.

8.1.3 Battery life
The device remains in deep sleep for most of the time, resulting in a current consumption as low as 5 mA. However, as shown in fig. 5.2, the ESP32 itself consumes only 0.15 mA in deep sleep mode. Therefore, most of the energy is used by the battery management system and the analog circuit.

Regarding power consumption during BLE data transmission, the current is approximately 40 mA. However, the actual data transmission and advertising process only last about one second, even though fig. 7.8 shows a total duration of around three seconds. This discrepancy arises because, in the Python script, the program requires additional time to prepare for receiving notifications from the ESP32 after a successful connection. If the ESP32 sends data too early, the computer may fail to receive the full dataset. To address this, we designed a simple protocol: once the connection is established, the computer initiates the preparation process for receiving notifications. After this preparation is complete, the computer sends a message to trigger the ESP32 to start data transmission. The entire process takes approximately two seconds.

Another limitation is the frequency of CPU wake-ups. In this device, the wake-up interval is approximately 17 seconds. This is due to the memory constraints of RTC_SLOW_MEM, where 1700 × 4 bytes are allocated for EEG data storage, with each sample occupying 32 bits in memory. The total size of RTC_SLOW_MEM is 8 KB, of which 6.5 KB is used for data storage, while the remaining portion is reserved for ULP code. As a result, at a sampling rate of 100 Hz, the RTC memory reaches full capacity within 17 seconds. If the ULP co-processor could utilize other peripherals, such as flash memory, the wake-up frequency could be further reduced, leading to lower power consumption.

8.2 Future
8.2.1 Improved Contact Design
Our EEG device demonstrates excellent wearability and flexibility, with a compact PCB and an integrated battery system. However, the current device size of approximately 8 × 8 cm² makes it difficult to wear comfortably, particularly around the hairline. A straightfor-

ward way to reduce its size is to split the PCB into two independent boards: one dedicated to the signal processing circuit and the other housing the MCU and battery system. These two boards can be connected using a cross-board connector, with a shielding layer in between to minimize interference from high-frequency components in the MCU. While this design doubles the device's height, it significantly enhances its suitability as a wearable device.

Additionally, the amplification circuits for all four channels currently occupy considerable PCB space, as each channel has a separate circuit. If we can reuse a single amplification circuit for all four channels, the overall size of the device will be significantly reduced. The main challenge in achieving this lies in designing an efficient channel-switching system and ensuring the ADC can handle rapid switching. The channel-switching mechanism could be implemented using NMOS transistors between the MCU pins and each channel, allowing channels to be selectively activated.

Regarding the ADC, the sampling rate must be significantly higher than that of a single channel. For instance, if four channels are combined into one, the required sampling rate is 4 × 250 = 1000 Hz, meaning a sample must be taken every 1 ms. However, the ADS1115 ADC has a maximum sampling rate of only 860 SPS, making it unsuitable for this approach. A new ADC with a higher sampling frequency should be considered. Furthermore, baseline differences between EEG channels could pose a challenge—if capacitors and op-amps fail to respond quickly to voltage changes within 1 ms, the recorded signal may become unusable. These issues must be addressed in future device miniaturization efforts.

Lastly, battery size remains a limiting factor. While the current design has already optimized power consumption by replacing a traditional dual-supply system with a single 3.7V Li-ion battery, further size reduction is possible. One potential solution is wireless charging via an inductive coil. With recent advancements in wireless charging for mobile devices, a 2 × 2 cm^2 coil could provide 5V power, which could then be regulated via a DC-DC converter and LDO to meet the voltage requirements of other components. However, the charging distance is limited to 3–5 cm, making it practical primarily for sleep EEG applications where the device can be charged under a pillow. Nevertheless, this technology holds promise, especially for future invasive EEG designs.

8.2.2 Better Wireless Transmission

As discussed in Section 5, we chose the ESP32 series over the nRF52 series primarily due to its superior Bluetooth communication capabilities. However, ESP32 also offers other wireless communication options, such as WiFi.

A major drawback of Bluetooth is that obstacles between the transmitter and receiver significantly degrade signal quality. In our tests, the effective wireless transmission distance was only about 20 cm, and signal quality deteriorated further when the device was placed behind a hat or a hard band. A better solution would be to utilize the WiFi module for more stable data transmission. However, WiFi consumes significantly more power than Bluetooth, making it unsuitable for long-term monitoring without optimization. Future research should explore low-power WiFi transmission methods to establish a more stable connection between the device and the computer while maintaining energy efficiency.

8.2.3 Further improvement at the conductive polymer material

In Section 7, we evaluated the performance of conductive polymer electrodes, but the results were not satisfactory. Despite this, conductive polymer materials remain highly promising for biomedical signal acquisition. Further testing is required to fully understand

their electrical properties.

For instance, the impedance of the conductive polymer material under AC voltage at different frequencies should be characterized. Additionally, the electrode shape needs further refinement. The current flat-plate design is not ideal for EEG acquisition in areas with hair. Alternative designs, such as claw- or nail-shaped electrodes, should be explored to improve contact with the scalp.

Before applying conductive polymer electrodes to EEG recording, testing them in an ECG setup may be more appropriate. ECG electrodes are placed on the chest and legs, where hair interference is minimal. Moreover, ECG signals are easier to identify in the time domain, making it simpler to assess electrode performance. Conducting ECG experiments first would provide a clearer evaluation of conductive polymer electrodes before transitioning to EEG applications.

9 Conclusion

In this thesis, we explored the design and optimization of a low-power, wearable EEG device. The potential use of a novel conductive polymer material was also tested to enhance the flexibility and biocompatibility of the device. This study aimed to address three main challenges in current EEG devices availale on market:

- (1) The development of a compact and wearable EEG signal recording device,
- (2) Long-term continuous monitoring at both hardware and firmware levels, and
- (3) The evaluation of common electrodes used in EEG signal acquisition, as well as the performance of conductive polymer electrodes in terms of impedance, signal quality, and convenience.

Our work began with circuit design. The entire EEG amplification and filtering circuit was built and designed from scratch. The selection of different component types, circuit topologies, and component values is discussed in detail. The circuit's performance was refined step by step, and suitable values were compared in terms of PCB size and noise reduction. The introduction of a filtering circuit and a Driven Right Leg (DRL) circuit further reduced noise in the recorded EEG signal. A simulation of the circuit, using models corresponding to the actual components, was conducted to verify expected performance. Finally a experiment is designed to verify the signal recorded by device is indeed the EEG signal. The PCB design was optimized not only for minimal space usage but also to separate the signal processing unit, MCU, and power supply system into different areas to reduce high-frequency noise from the MCU. Unlike traditional dual power supplies that use two independent batteries, our power system utilizes a single battery, along with DC-DC converters and LDO circuits, to generate the necessary voltages for other components. This approach balances device size and battery life.

Beyond hardware, this study also introduced firmware-level optimizations. The MCU's operation was extensively refined using the official ESP-IDF (Espressif IoT Development Framework), reducing power consumption much lower than the Arduino-based scripts. By optimizing the communication protocol between the MCU and ADC, the device can operate with the ADC in deep sleep mode, significantly lowering power consumption. These optimizations were implemented in assembly language, ensuring high algorithmic efficiency. The main CPU wakes at specific intervals to transmit data via BLE to a computer, dramatically extending battery life compared to currently available wearable EEG devices.

To evaluate the feasibility of conductive polymer electrodes as substitutes for traditional wet/gel electrodes, experiments were conducted comparing signal quality between wet/gel electrodes, dry electrodes, and conductive polymer electrodes. The results showed that wet/gel electrodes provided satisfactory signal quality but required complex setup procedures and reapplication for long-term use. Dry electrodes were easier to use but exhibited higher noise and weaker attachment compared to wet/gel electrodes. The conductive polymer electrodes, however, did not yield usable data. We hypothesize that this is due to the size and shape of the sample electrodes, which may not be suitable for EEG signal acquisition, particularly in areas with hair. Additionally, the conductive polymer material required water application before use to modify its properties, which may have led

to unstable electrical performance. Further research is needed to assess the viability of conductive polymers as biomedical signal sensors.

Despite the advancements presented in this thesis, there are still limitations and areas for improvement. Further miniaturization is possible, such as integrating the four identical amplification circuits into a single unit and using an NMOS circuit controlled by the MCU for channel switching. Wireless charging, commonly used in mobile devices, could also be explored. While the low-power consumption significantly extends battery life, Bluetooth communication stability remains a challenge. Alternative wireless communication methods, such as WiFi, should be considered. Additionally, the signal processing pipeline could be enhanced with advanced algorithms, such as eye movement artifact removal or feature recognition.

In conclusion, this study has demonstrated that a wearable EEG device capable of long-term continuous monitoring can be developed through careful circuit design, optimized power management, and firmware-level enhancements. However, the performance of conductive polymer electrodes still requires further research. These findings contribute not only to the development of wearable EEG devices but also to other biomedical signal acquisition systems requiring low power consumption and wireless communication.

Bibliography

[1] Andrea Biasiucci, Benedetta Franceschiello, and Micah M. Murray. “Electroencephalography”. In: *Current Biology* 29.3 (2019), R80–R85. ISSN: 0960-9822. DOI: https://doi.org/10.1016/j.cub.2018.11.052. URL: https://www.sciencedirect.com/science/article/pii/S0960982218315513.

[2] Mera kartika delimayanti et al. “Classification of Brainwaves for Sleep Stages by High-Dimensional FFT Features from EEG Signals”. In: *Applied Sciences* 10 (Mar. 2020). DOI: 10.3390/app10051797.

[3] Kaido Värbu, Naveed Muhammad, and Yar Muhammad. “Past, Present, and Future of EEG-Based BCI Applications”. In: *Sensors* 22.9 (2022). ISSN: 1424-8220. DOI: 10.3390/s22093331. URL: https://www.mdpi.com/1424-8220/22/9/3331.

[4] Maria E Peltola et al. “Routine and sleep EEG: Minimum recording standards of the International Federation of Clinical Neurophysiology and the International League Against Epilepsy”. en. In: *Epilepsia* 64.3 (Mar. 2023), pp. 602–618.

[5] Richard W Homan, John Herman, and Phillip Purdy. “Cerebral location of international 10–20 system electrode placement”. In: *Electroencephalography and Clinical Neurophysiology* 66.4 (1987), pp. 376–382. ISSN: 0013-4694. DOI: https://doi.org/10.1016/0013-4694(87)90206-9. URL: https://www.sciencedirect.com/science/article/pii/0013469487902069.

[6] Sándor Beniczky and Donald L Schomer. “Electroencephalography: basic biophysical and technological aspects important for clinical applications”. en. In: *Epileptic Disord.* 22.6 (Dec. 2020), pp. 697–715.

[7] Marcus C Ng, Jin Jing, and M Brandon Westover. “A primer on EEG spectrograms”. en. In: *J. Clin. Neurophysiol.* 39.3 (Mar. 2022), pp. 177–183.

[8] Xiao Jiang, Gui-Bin Bian, and Zean Tian. “Removal of artifacts from EEG signals: A review”. en. In: *Sensors (Basel)* 19.5 (Feb. 2019), p. 987.

[9] Xiashuang Wang et al. “Automated recognition of epilepsy from EEG signals using a combining space-time algorithm of CNN-LSTM”. en. In: *Sci. Rep.* 13.1 (Sept. 2023), p. 14876.

[10] Anteneh M. Feyissa and William O. Tatum. “Chapter 7 - Adult EEG”. In: *Clinical Neurophysiology: Basis and Technical Aspects*. Ed. by Kerry H. Levin and Patrick Chauvel. Vol. 160. Handbook of Clinical Neurology. Elsevier, 2019, pp. 103–124. DOI: https://doi.org/10.1016/B978-0-444-64032-1.00007-2. URL: https://www.sciencedirect.com/science/article/pii/B9780444640321000072.

[11] Ning-Han Liu, Cheng-Yu Chiang, and Hsuan-Chin Chu. “Recognizing the degree of human attention using EEG signals from mobile sensors”. en. In: *Sensors (Basel)* 13.8 (Aug. 2013), pp. 10273–10286.

[12] Neha Sharma et al. “Deep temporal networks for EEG-based motor imagery recognition”. en. In: *Sci. Rep.* 13.1 (Nov. 2023), p. 18813.

[13] T.A. Suhail et al. “Distinguishing cognitive states using electroencephalography local activation and functional connectivity patterns”. In: *Biomedical Signal Processing and Control* 77 (2022), p. 103742. ISSN: 1746-8094. DOI: https://doi.org/10.1016/j.bspc.2022.103742. URL: https://www.sciencedirect.com/science/article/pii/S1746809422002646.

[14] Marcel van Gerven et al. “The brain–computer interface cycle”. In: *Journal of neural engineering* 6 (Sept. 2009), p. 041001. DOI: 10.1088/1741-2560/6/4/041001.

[15] Andrea Biondi et al. “New wearable and portable EEG modalities in epilepsy: The views of hospital-based healthcare professionals”. In: *Epilepsy Behavior* 159 (2024), p. 109990. ISSN: 1525-5050. DOI: https://doi.org/10.1016/j.yebeh.2024.109990. URL: https://www.sciencedirect.com/science/article/pii/S1525505024003718.
[16] Alexander J Casson. “Wearable EEG and beyond”. en. In: *Biomed. Eng. Lett.* 9.1 (Feb. 2019), pp. 53–71.
[17] Genaro Rebolledo-Mendez et al. “Assessing NeuroSky’s Usability to Detect Attention Levels in an Assessment Exercise”. In: July 2009, pp. 149–158. ISBN: 978-3-642-02573-0. DOI: 10.1007/978-3-642-02574-7_17.
[18] Yangting Zhang et al. “Minimal EEG channel selection for depression detection with connectivity features during sleep”. In: *Computers in Biology and Medicine* 147 (2022), p. 105690. ISSN: 0010-4825. DOI: https://doi.org/10.1016/j.compbiomed.2022.105690. URL: https://www.sciencedirect.com/science/article/pii/S0010482522004759.
[19] Xuanqin Yu. *EEG device related files*. https://github.com/XuanqinYu/eegDevice_DTU. 2025.
[20] C. S. Nayak and A. C. Anilkumar. *EEG Normal Waveforms*. StatPearls [Internet]. Updated 2023 Jul 24. Available at: https://www.ncbi.nlm.nih.gov/books/NBK539805/. Treasure Island (FL), 2025. URL: https://www.ncbi.nlm.nih.gov/books/NBK539805/.
[21] Jiawei Xu et al. “Active electrodes for wearable EEG acquisition: Review and electronics design methodology”. In: *IEEE Rev. Biomed. Eng.* 10 (2017), pp. 187–198.
[22] Firoz Babu Kadumudi et al. “The manufacture of unbreakable bionics via multifunctional and self-healing silk-graphene hydrogels”. en. In: *Adv. Mater.* 33.35 (Sept. 2021), e2100047.
[23] Matteo Paolieri et al. “Biomimetic Flexible Electronic Materials from Silk Fibroin-MXene Composites Developed via Mussel-Inspired Chemistry as Wearable Pressure Sensors”. In: *ACS Applied Nano Materials* 6.7 (2023), pp. 5211–5223. DOI: 10.1021/acsanm.2c05140. eprint: https://doi.org/10.1021/acsanm.2c05140. URL: https://doi.org/10.1021/acsanm.2c05140.
[24] Thomas Stone. “Chapter 11 - Medical Electronics”. In: *Clinical Engineering*. Ed. by Azzam Taktak et al. Oxford: Academic Press, 2014, pp. 193–210. ISBN: 978-0-12-396961-3. DOI: https://doi.org/10.1016/B978-0-12-396961-3.00011-1. URL: https://www.sciencedirect.com/science/article/pii/B9780123969613000111.
[25] Texas Instruments. *INA333 Low-Power, Precision Instrumentation Amplifier Datasheet*. Version Rev. F. Texas Instruments. Dallas, TX, USA, Mar. 2025. URL: http://www.ti.com/lit/ds/symlink/ina333.pdf (visited on 02/15/2025).
[26] Federico N. Guerrero and Enrique Spinelli. “High gain driven right leg circuit for dry electrode systems”. In: *Medical Engineering Physics* 39 (2017), pp. 117–122. ISSN: 1350-4533. DOI: https://doi.org/10.1016/j.medengphy.2016.11.005. URL: https://www.sciencedirect.com/science/article/pii/S1350453316302806.
[27] N Agarwal et al. “Portable cost-effective EEG data acquisition system”. en. In: *J. Med. Eng. Technol.* 35.3-4 (Apr. 2011), pp. 185–190.
[28] Alan S. Morris and Reza Langari. “Chapter 8 - Principles of data acquisition and signal processing”. In: *Measurement and Instrumentation (Third Edition)*. Ed. by Alan S. Morris and Reza Langari. Third Edition. Academic Press, 2021, pp. 211–241. ISBN: 978-0-12-817141-7. DOI: https://doi.org/10.1016/B978-0-12-817141-7.00008-6. URL: https://www.sciencedirect.com/science/article/pii/B9780128171417000086.
[29] James I. Grossman and Abner J. Delman. “Serial P wave changes in acute myocardial infarction”. In: *American Heart Journal* 77.3 (1969), pp. 336–341. ISSN: 0002-8703. DOI: https://doi.org/10.1016/0002-8703(69)90189-6. URL: https://www.sciencedirect.com/science/article/pii/0002870369901896.

[30] Texas Instruments. *Analysis of the Sallen-Key Architecture Application Report*. Texas Instruments. Dallas, TX, USA, Mar. 2025. URL: https://www.ti.com/lit/an/sloa024b/sloa024b.pdf?ts=1742216229693&ref_url=https%253A%252F%252Fwww.google.com%252F (visited on 02/15/2025).

[31] Texas Instruments. *1.8-V, microPower, CMOS Operational Amplifiers, Zero-Drift Series*. Texas Instruments. Dallas, TX, USA, Mar. 2025. URL: https://www.lcsc.com/datasheet/lcsc_datasheet_1809200040_Texas-Instruments-OPA2333AIDR_C38732.pdf (visited on 02/15/2025).

[32] Texas Instruments. *Active Low-Pass Filter Design*. Texas Instruments. Dallas, TX, USA, Mar. 2025. URL: https://d1.amobbs.com/bbs_upload782111/files_46/ourdev_680014SMMOSW.pdf (visited on 02/15/2025).

[33] Manon Kloosterman et al. "Body Surface Potential Mapping Detects Early Disease Onset in PKP2-Pathogenic Variant Carriers". In: *Europace* 25 (July 2023). DOI: 10.1093/europace/euad197.

[34] Ali Bulent Usakli. "Improvement of EEG signal acquisition: an electrical aspect for state of the art of front end". en. In: *Comput. Intell. Neurosci.* 2010 (Feb. 2010), p. 630649.

[35] Texas Instruments. *Ultra-Small, Low-Power, 16-Bit Analog-to-Digital Converter with Internal Reference*. Texas Instruments. Dallas, TX, USA, Mar. 2025. URL: https://www.lcsc.com/datasheet/lcsc_datasheet_1809192322_Texas-Instruments-ADS1115IDGSR_C37593.pdf (visited on 02/15/2025).

[36] Texas Instruments. *LM27762 Low-Noise Positive and Negative Output Integrated Charge Pump Plus LDO*. Texas Instruments. Dallas, TX, USA, Mar. 2025. URL: https://www.ti.com/lit/ds/symlink/lm27762.pdf (visited on 02/15/2025).

[37] TOREX SEMICONDUCTOR LTD. *Low ESR Cap.Compatible Positive Voltage Regulators*. TOREX SEMICONDUCTOR LTD. Tokyo, Japan, Mar. 2025. URL: https://jlcpcb.com/api/file/downloadByFileSystemAccessId/8579707861620228096 (visited on 02/15/2025).

[38] Nordic Semiconductor. *nRF52840 Product Specification v2.0*. Version Rev. 2. Nordic Semiconductor ASA. Oslo, Norway, Jan. 2021. URL: https://docs-be.nordicsemi.com/bundle/ps_nrf52840/attach/nRF52840_PS_v1.11.pdf?_LANG=enus (visited on 03/20/2024).

[39] Espressif Systems. *ESP32 Technical Reference Manual*. Tech. rep. Accessed: 2024-02-15. Espressif Systems, 2020. URL: https://www.espressif.com/sites/default/files/documentation/esp32_technical_reference_manual_en.pdf.

[40] Amjed S Al-Fahoum and Ausilah A Al-Fraihat. "Methods of EEG signal features extraction using linear analysis in frequency and time-frequency domains". en. In: *ISRN Neurosci.* 2014 (Feb. 2014), p. 730218.

[41] Radwa Reda et al. "Analyzing electrooculography (EOG) for eye movement detection". en. In: *Advances in Intelligent Systems and Computing*. Advances in intelligent systems and computing. Cham: Springer International Publishing, 2020, pp. 179–189.

[42] Satya Muddamsetty. "Spatio-temporal saliency detection in dynamic scenes using color and texture features". In: (July 2014).

A Appendix

A.1 ulp.S

```
#include "soc/soc_ulp.h"
#include "soc/rtc_cntl_reg.h"
#include "soc/rtc_io_reg.h"
#include "soc/sens_reg.h"
#include "soc/rtc_i2c_reg.h"

#include "stack.S"


#define N_SAMPLE      1700

.bss
.global buffer_index
buffer_index:
    .align 4
    .long 0

.global data_buffer
data_buffer:
    .align 4
    .space 4*N_SAMPLE

.global doread
doread:
    .align 4
    .long 0

.global stackEnd
stackEnd:
    .long 0

.text
.global entry
entry:
    // check if in continuous mode
    move r1, doread
    ld r0, r1, 0
    jumpr readvalue, 1, ge

    // write config
    move r3, stackEnd
    psr
    jump i2c_start_cond

    move r2, 0x90
    move r1, 0x00
    psr
    jump i2c_write_byte
    jumpr noack, 1, ge

    move r2, 0x01
    psr
    jump i2c_write_byte
    jumpr noack, 1, ge

```

```
    move r2, 0xC2
    psr
    jump i2c_write_byte
    jumpr noack, 1, ge

    move r2, 0xe3
    psr
    jump i2c_write_byte
    jumpr noack, 1, ge

    psr
    jump i2c_stop_cond

    wait 100000

    // write read mode
    psr
    jump i2c_start_cond

    move r2, 0x90
    psr
    jump i2c_write_byte
    jumpr noack, 1, ge

    move r2, 0x00
    psr
    jump i2c_write_byte
    jumpr noack, 1, ge

    psr
    jump i2c_stop_cond

    move r1, doread
    move r0, 0x02
    st r0, r1, 0

readvalue:
    psr
    jump i2c_start_cond
    move r2, 0x91
    psr
    jump i2c_write_byte
    jumpr noack, 1, ge

    psr
    jump i2c_read_byte
    push r0
    move r2,1
    psr
    jump i2c_read_byte
    push r0
    psr
    jump i2c_stop_cond

    pop r0
    pop r2
    lsh r2,r2,8
    or r2,r2,r0
    move r3,r2

finish:
    MOVE r1, buffer_index
```

```
    MOVE r2, data_buffer

    LD r0, r1, 0

    ADD r2, r2, r0
    ST r3, r2, 0

    ADD r0, r0, 1
    ST r0, r1, 0

check:
    //move r3, N_SAMPLE
    //sub r3, r0, r3
    jumpr buffer_full, N_SAMPLE, ge

.global exit
exit:
  halt

.global buffer_full
buffer_full:
  READ_RTC_FIELD(RTC_CNTL_LOW_POWER_ST_REG, RTC_CNTL_RDY_FOR_WAKEUP)
  and r0, r0, 1
  jump exit, eq

  /* Wake up the SoC, end program */
  wake
  WRITE_RTC_FIELD(RTC_CNTL_STATE0_REG, RTC_CNTL_ULP_CP_SLP_TIMER_EN, 0)
  halt

noack:
    move r3, 99
    jump finish
```

Listing A.1: Complete code for I2C communication using ULP co-processor.

This device is developed under the constriction and sponsored by DTU. The main contributor (Xuanqin Yu), supervisors and DTU share the patent or utility model of the device. Anyone should not put it into commercial activity without the permission from above stakeholders.

update: 2025/03/17

Technical
University of
Denmark

Brovej, Building 423
2800 Kgs. Lyngby
Tlf. 4525 1700

https://www.healthtech.dtu.dk/